Version of Record: https://www.sciencedirect.com/science/article/pii/S0955221920301734
Manuscript_8521a7962005c97e4b78ab5dce26f271

Synthesis and Properties of macroporous SiC Ceramics synthesized by 3D printing and chemical vapor infiltration/deposition

A. Baux[1], A. Goillot[1], S. Jacques[1], C. Heisel[2], D. Rochais[2], L. Charpentier[3], P. David[2], T. Piquero[2], T. Chartier[4], G. Chollon[1*]

[1] LCTS-CNRS, 3, allée de la Boétie, 33600 Pessac, France

[2] CEA-DAM, Le Ripault, 37260 Monts, France

[3] PROMES-CNRS, 7 rue du four solaire, 66120 Font-Romeu Odeillo, France

[4] IRCER-CNRS, Centre Européen de la Céramique, 12 Rue Atlantis, 87068 Limoges, France

**Corresponding author. E-mail: chollon@lcts.u-bordeaux.fr*

Abstract: Open porosity cellular SiC-based ceramics have a great potential for energy conversion, e.g. as solar receivers. In spite of their tolerance to damage, structural applications at high temperature remain limited due to high production costs or inappropriate properties. The objective of this work was to investigate an original route for the manufacturing of porous SiC ceramics based on 3D printing and chemical vapor infiltration/deposition (CVI/CVD). After binder jetting 3D-printing, the green α-SiC porous structures were reinforced by CVI/CVD of SiC using CH_3SiCl_3/H_2. The multiscale structure of the SiC porous specimens was carefully examined as well as the elemental and phase content at the microscale. The oxidation and thermal shock resistance of the porous SiC structures and model specimens were also studied, as well as the thermal and mechanical properties. The pure and dense CVI/CVD-SiC coating considerably improves the mechanical strength, oxidation resistance and thermal diffusivity of the material.

Keywords: Binder jetting; Silicon carbide; Polymer-derived ceramics (PDC); Chemical vapor deposition (CVD); Thermomechanical properties

1. Introduction

The increasing problem of CO_2 emissions and energy security concerns such as nuclear safety, radioactive waste management and resource dependence, have given interest in alternative sources of energy. Solar energy is unlimited and clean, and concentrated solar power (CSP) using optical concentration is a particularly good candidate for providing a clean and renewable source of energy [1, 2]. In CSP systems, the solar radiation is converted into heat by a solar receiver, which is passed through a heat transfer fluid. Volumetric solar receivers (VSR) are probably the most efficient variety of solar receivers. These macroporous cellular ceramics can

© 2020 published by Elsevier. This manuscript is made available under the Elsevier user license
https://www.elsevier.com/open-access/userlicense/1.0/

achieve particularly high energy efficiency thanks to the so-called volumetric effect, characterized by (i) a temperature of the solid that is higher at the exit than at the entrance and (ii) a temperature of the fluid that reaches that of the solid at the exit [3, 4, 5]. The volumetric effect can be attained only by finding the best compromise in terms of pore volume geometry (e. g. cell shape and size) and material properties (e. g. optical selectivity, mechanical strength/stiffness, thermal conductivity/expansion, oxidation resistance). The pore volume geometry of VSR is currently very limited, mostly due to fabrication constrains. Two major types can be found: extruded structures such as honeycombs [6, 7] and open foams made by replication [7, 8, 9, 10, 11]. For both categories, the geometrical pattern, the cell size and the open porosity are not easily adjustable, so a satisfactory compromise is difficult to find. Another type of cellular ceramics is 3D lattice structures. These synthetic structures are often periodic (yet not necessarily: [12]), but non-extrudable. Provided they can be effectively fabricated, they could be designed specifically to demonstrate the volumetric effect [13]. In order to improve the performance of VSR, it would be then beneficial to turn to a manufacturing method that is able to generate any morphology and especially those likely to demonstrate the volumetric effect. The rapid growth of 3D printing in recent years has led us to consider this technology as a practical solution.

The basic principle of 3D printing –or additive manufacturing– is to generate a 3D computer-assisted design (CAD) model to directly manufacture a three-dimensional object layers by layers. Technologies such as selective laser sintering, fused deposition modeling and stereolithography were initially developed for polymer materials [14]. They were successfully adapted to 3D ceramic parts only a few years later [15, 16, 17]. Binder jetting (BJ) is another technique derived from inkjet printing that was soon applied to produce green ceramic parts before sintering [18]. Finally, robocasting, based on the extrusion of a filament from a paste, was also used for the fabrication of simple 3D ceramic structures after sintering [19]. All of these techniques and a few others were employed as at least one step in the manufacturing of complex shaped ceramics [14, 20, 21]. Thermal post-treatments are indeed often required to obtain dense ceramic parts. These final ceramization/densification stages depend on the nature of the ceramic itself.

The solid material constituting the porous structure of VSR must resist to oxidation at high operating temperatures in air (typically around 1000 °C, but up to 1200-1300 °C [4, 6, 8]) and supposedly for very long periods of time. It has also to absorb a maximum of solar radiation, emit a minimum of IR thermal radiation, diffuse sufficiently heat and, finally, resist to thermal

shock, i.e. meet a subtle combination of high strength, low stiffness, low coefficient of thermal expansion (CTE) and high thermal conductivity [22]. These very strict –sometimes conflicting– requirements rule out metals and oxides and put forward silicon carbide (SiC), which is still considered as the reference material for an application as VSR [4, 6, 7, 11, 23, 24, 25].

3D SiC-based structures were prepared by using the different additive manufacturing techniques mentionned above (except direct selective laser sintering), but the processing routes followed are often multi-step and hybrid. For instance, Ortona *et al.* produced Si-SiC cellular ceramics by replication, with a ceramic slurry, of a polymer structure printed by strereolithography, firing and liquid silicon infiltration (LSI) [26]. Similarly, Wahl *et al.* densified by LSI relatively complex shapes –yet, with a rougher surface finish– made by robocasting [27]. Schlier *et al.* or Fleisher *et al* also used LSI, but after BJ on a SiC powder bed of a water-based solution containing a carbon precursor [28, 29], or after BJ and polymer impregnation and pyrolysis (PIP) with a phenolic resin [30]. Preceramic polymers can also be used as raw materials for printing as an alternative to SiC powders. Zocca *et al.* indeed synthesized Si-O-C ceramics by BJ of solid precursors and pyrolysis [31]. Liquid preceramic polymers were also modified to become UV curable and suitable for stereolithography, resulting in Si-O-C or SiC-based ceramics after pyrolysis [32, 33]. Most of these routes leads to a poor SiC crystallinity and a high amount of impurities in the final material: e. g. free silicon after LSI, or free turbostratic carbon –sometimes even combined with an amorphous silicon oxycarbide phase– when starting from preceramic polymers. These microstructures could be sources of thermochemical instability, high susceptibility to oxidation, corrosion and creep, and finally a low level of thermal conductivity. It is indeed known to what extent the overall properties of SiC-based materials vary according to their purity, microstructure and structure [34].

Our approach is to take advantage of the ease of 3D printing for the formatting of complex shaped cellular materials, but not at the expense of the solid constituent purity. We therefore oriented our choice towards binder jetting 3D printing because it respects the purity of the starting SiC powder. The first original aspect of our work is the deliberate introduction of a high multiscale residual porosity into the printed and fired material. This is achieved by adding a pore forming agent to the SiC powder bed and by an intermediate PIP step to consolidate the SiC porous body. The second main feature of this method is the use of chemical vapor infiltration and deposition (CVI, CVD) to fill in the residual microporosity and cover up the solid with pure and crystalline SiC. This process has been studied and used for many years [35,

36, 37] and CVD-SiC is recognized as a high performance material whose properties are very well documented [34].

The first main objective of this work is to examine the feasibility and understand the various stages of the process along the synthesis of a model SiC-based 3D lattice structure. The composition and the microstructure of the solid and the porous network will be analyzed in details at different scales.

The second objective is to evaluate the various intrinsic properties of the constituting SiC-based material that are most relevant to the application as VSR, namely, mechanical properties, oxidation resistance, thermo-physical properties, thermal expansion, thermal micro-diffusivity and thermal shock resistance. These tests will be performed at the various stages of the process, mostly on model specimens.

The optimization of the VSR 3D structures by numerical simulation and the evaluation of their macroscopic properties, in conditions close to the application, is not to be addressed here but will appear in a forthcoming paper.

2. Experimental procedure

2.1. Sample processing

2.1.1. 3D printing: binder jetting, polymer impregnation and pyrolysis

The method used to build the samples is based on two steps: the porous 3D SiC structure is obtained in a first step the first step by binder jetting and the second step consists of various post-treatments to obtain the final part. The binder jetting process belongs to the family of indirect Additive Manufacturing technologies [20, 21]. It has the first advantage of not requiring the use of a supporting structure, whatever the shape and size of the object, but is not able to manufacture parts with a low porosity and closed pores. The printer used was a Zprinter 310+ from Z Corporation. This printer is composed of two juxtaposed tanks, both equipped with a piston driven plate. The first tank is called the “feed tank” and the other is the “build tank”. Initially, the feed tank was filled with powder with the plate in the down position, while the plate of the build tank was in the up position. To print a layer, the feed plate was raised up to 100 µm and simultaneously the build plate was lowered by 100 µm, such a height corresponding to the thickness of a single deposition layer. A roller spreads the powder from the feed tank to deposit a 100 µm thick powder bed on the build tank. The binder solution (ProBinder 20,

composed of more than 95 % of water) was then applied by a print head on the freshly spread powder bed in order to bind particles in the cross-sectional pattern indicated by the CAD file. To promote the binding between the particles, printing took place at a temperature of about 40 °C. After printing the last layer and a waiting period of one hour, the agglomerated part was removed from the powder. The raw solid parts were printed from a mixture of plaster as a binder and α-SiC powder with an average particle diameter of 25 µm (ref. 357391, Sigma Aldrich). In the second step, the porous raw parts were impregnated at room temperature (RT) with a liquid polymeric SiC precursor and more precisely an allyhydridopolycarbosilane (AHPCS, tradename: SMP-10, from Starfire Systems, Inc, USA). This polymer precursor was chosen because of its high ceramic yield of at least 70 wt % [38, 39]. The precursor impregnated in the raw parts was cured in air at 250 °C (heating ramp 100 °C/h) during two hours to consolidate the material before the further treatments. The precursor-to-ceramic conversion was achieved by pyrolyzing the impregnated parts under flowing argon (Alphagaz 2 from Air Liquide, 10^5 Pa) with a constant heating rate of 100 °C/h and a dwell time of 1 h at 1000 °C. A single polymer impregnation and pyrolysis (PIP) cycle and no particular curing stage were carried out because a complete densification was not needed here, contrary to the matrix processing for ceramic matrix composites [40]. The parts being sufficiently consolidated by PIP, the plaster binder was removed by dipping the part in an HCl aqueous solution.

This technique was used to manufacture the cellular lattice structures, but also two types of model specimens dedicated to specific tests: solid rods and circular plates. The lattice structure is composed of cubic unit cells (Fig. 1.a) periodically repeated six times in all three directions (Fig. 1.b). The cubic cells have a width of 5 mm and the cell edge struts have a cylindrical section of a diameter of 1.3 mm. The linking nodes between struts are spherical with a radius of 1.2 mm. The particular shape of the lattice structures makes sometimes difficult the characterization of the solid material constituting the struts. In this respect, model materials were printed with a more basic rod shape (Fig. 1.c). In order to be easily handled after 3D printing, the rods had to be larger in diameter than the struts of lattice structure. After the printing process, the raw rods were straight, 50 mm long and had a circular cross-section of a diameter of 2.3 mm as expected from the CAD file. Yet, after the various post-treatments, the sections of the rods became elliptical and some of them were slightly curved (Fig. 1.c). These geometrical deformations were probably due to a heterogeneous distribution of the AHPCS after the impregnation and thus to some differential shrinkage during pyrolysis.

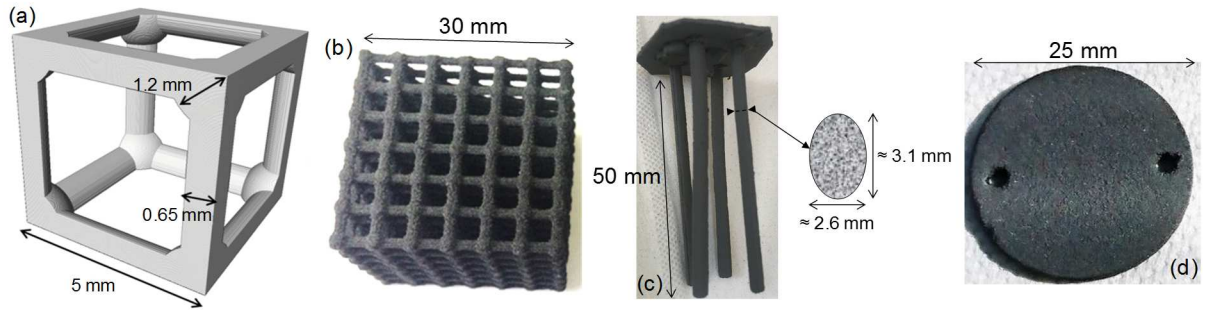

Fig. 1. Specimens processed and tested: (a) cubic unit cell (b) cellular lattice structures, (c) rods, (d) circular plates

Some surface or in-depth characterization techniques required larger and flat specimens. Circular plates were then printed with a diameter of 25 mm and a thickness of 2 mm. Some of them were printed with two small symmetrical holes near the edge, while the others had one small hoop, to facilitate hanging during the subsequent step of the process.

After the binder jetting printing and PIP steps, the so-called "PIP" specimens obtained were found to have a strength. They were then submitted to either one or two additional processing steps of chemical vapor infiltration or deposition (CVI/CVD) for further densification and strengthening.

2.1.2. Chemical vapor infiltration and deposition

The CVI/CVD reactor consisted of a sintered silicon carbide tube, with an inner diameter of 63.5 mm. The SiC tube was installed inside a high temperature electrical resistive furnace (Carbolite STF1500) having a 600 mm long hot zone. In a first step, a thin SiC coating was deposited by CVI on the PIP specimens at moderate temperature (*T*) and low pressure (*P*) (see Table 1). These low growth rate conditions (1 µm/h) were selected to promote infiltration into the strut microporosity of the lattice structures (the term “microporosity” here does not refer to the IUPAC nomenclature for carbon materials but simply to a porosity at the micrometer scale). It is worth mentioning that the PIP rods and circular plates were not submitted to this first CVI stage. A final CVD step at higher temperature and pressure (Table 1) was performed to complete the reinforcement of the lattice structures (after CVI) and the model rods and plates (after PIP). The conditions were in this case adapted for a SiC deposition at high growth rate (14 µm/h).

For both CVI and CVD steps, the SiC deposit was produced from a mixture of methyltrichlorosilane (MTS) and hydrogen. The gas flow rates Q_{MTS} and Q_{H2} were controlled by mass flowmeters (SLA5850 from Brooks) with a H_2/MTS molar ratio of three. MTS was evaporated from a stainless steel vessel and diluted in H_2 (Alphagaz 2 from Air Liquide), the whole system being placed in an oven heated at 35 °C.

A rotary vane vacuum pump was connected to evacuate gases at the outlet of the reactor. Liquid nitrogen traps were installed upstream from the pump to condense corrosive by-products such as HCl. A schematic of the CVI/CVD device is available in [41]. A flexible graphite foil (Papyex ®) was placed against the inner side of the reactor wall to protect the SiC tube. The lattice structure was hung with a graphite frame and a thin molybdenum wire threaded through the open cells. One end of the rods was stuck with carbon glue to a graphite foil (Papyex ®) before being suspended in the reactor. The circular plates were assembled together and to the sample holder through their holes and hoops. All the specimens with their holders were placed in the center of the hot zone, where a homogeneous deposition rate is observed. Most of the samples were kept in the reactor between the CVI and the CVD step. Yet, few of them were taken out to control the SiC infiltration after the CVI step.

2.2. Characterization

The phase identification and the structural state of the samples were evaluated by Raman microspectroscopy (RMS, Labram HR, from Horiba-Jobin Yvon, λ = 632.8 nm, magnification ×100, acquisition time 2 × 5 s). The spectra are presented without baseline correction or intensity normalization for comparison. Scanning electron microscopy (SEM, FEI, Quanta 400 FEG) was used in the secondary electron (SE) mode to observe the surface morphology of the specimens. The samples were also embedded in epoxy resin, polished and examined by optical microscopy at various magnifications (LEICA wild VM3Z and Reichert-Jung MF3). The local composition of each constituent of the microstructure was examined by electron probe microAnalysis (EPMA - SX 100 CAMECA, source:15 kV, 20 nA). The Si and O weight concentrations were quantified with respectively LPET and PC1 crystals and the C concentration calculated by difference (SiC and SiO_2 were used as standards). The 3D architecture of the PIP and CVI/CVD lattice structures were analyzed by X-ray tomography (GE v|tome|x s research edition). The analyses were performed using a directional source (200 kV, 300 µA), an exposure time of 500 ms and a set of 2000 radiographs over 360 °. Two

different types of scan were recorded, at low resolution (23 µm) for modeling the total volume of the samples and at high resolution (2 µm) for a local analyze of a sample strut. The amount of porosity in the samples P_{tomo} was determined from the void to solid surface ratio after binarizing the cross-sectional images. The true density ρ_{true}^{He} of the PIP and CVI/CVD lattice structures was determined by He-pycnometry (He pycnometer AccuPyc 1330). The pore diameter distribution and the apparent density ρ_{app}^{Hg} of the solid part of the lattice structures (including microporosity), were determined by Hg-porosimetry (Autopore IV 9500 - Micromeritics). The open porosity P_{pycno} was calculated by combining the results of both He-pycnometry and Hg-porosimetry and using Eq. (1).

$$P_{pycno}\,(\%) = \frac{\rho_{true}^{He} - \rho_{app}^{Hg}}{\rho_{true}^{He}}\,100 \qquad (1)$$

Specific surface area (S_s) measurements were carried out by the BET (Brunauer, Emmett and Teller) method (Micromeritics Tristar 3000), using nitrogen (N_2) as the adsorbed species.

The mechanical properties of the materials were evaluated by several complementary techniques. Three post-CVD rods were subjected to non-destructive acoustic analysis to determine their elastic modulus, as based on the ASTM E1876-01 [42] Standard. The samples were held between two nylon wires precisely set at the fundamental vibration nodes (SupMat 1.). A sound vibration was generated by striking the center of the sample with a tiny hammer. The acoustic signal versus time was acquired with a microphone and the natural frequency f_f was determined by Fourier transform. The ASTM method for solid cylindrical rods was validated by testing pure and dense alumina rods (Al23 from Degussit) of a diameter of 3 mm. In the current case, however, the rods had an elliptical cross-section leading to two distinct natural frequencies (SupMat. 2). The elastic modulus was then deduced by identifying the two natural modes, as calculated by the finite element method (FEM), assuming the material isotropic.

4-point bending tests were also performed to complement acoustic analysis and determine the failure strength of the PIP and CVD rods at RT. The procedure was based on the ASTM C1684-13 standard [43]. A schematic of the device is given in SupMat 3.a. The pins were supposed punctual and the stresses due to friction were neglected. The flexural modulus (E_{bend}) and the failure stress (σ_{bend}) were determined by assuming the material isotropic and homogeneous, and by considering the geometric parameters of the specimen and the testing apparatus (length between external (L =36 mm) and internal supports (L/2), major (horizontal) and minor

(vertical) diameters of the elliptical cross-section of the rod, respectively D_h and D_v) [44], according to Eq. (2) and Eq. (3):

$$E_{bend} = \frac{2PL^3}{3\pi\Delta D_v^3 D_h} \quad (2)$$

$$\sigma_{bend} = \frac{4PL}{\pi D_v^2 D_h} \quad (3)$$

where P is the total load applied on the pins ($P = 2F$, with F the load applied on each pin) and Δ the displacement between the internal and external pins. The 4-point bending device is presented in SupMat 3.b. and SupMat 3.c. The main characteristics of the equipment used were an Instron 4505 testing machine, an Instron strain gauge with amplitude of +/- 5 mm and an Instron 1000 N load cell. The crosshead speed was 0.05 mm/min. Δ was determined by image correlation. Optical images were acquired with a CCD Hamamatsu camera and the CorreliSTC® software developed by HOLO3 was used for image correlation. The position of the various pins was recorded every ten seconds. Each of the successive images was compared with the reference image, taken before the deformation. Image correlation was applied to the pins and the surrounding device. A speckle pattern (black spotted white) was painted on each pin to minimize the error in the calculation of pixel displacement SupMat 3.c. Flexural tests were performed on the same alumina rods as above to validate the measurement of Δ.

A qualitative –and more technological– type of test was also carried out to evidence the strengthening of the lattice structures related to the CVI/CVD steps (Fig. 2.a.). This test was inspired by the work of Brezsny *et al.* who measured the single-strut tearing resistance of reticulated open cell ceramic foams [45]. A holding cage was assembled with two aluminum plates connected with two threaded rods. The top plate was drilled with a hole of one centimeter in diameter (greater than the length of a strut), allowing the passage of a nylon yarn, which was threated around one strut located on the top of the structure (Fig. 2.b). On the upper part of the assembly, the other end of the nylon loop was attached to a steel hook suspended to the upper crosshead of the tensile-testing machine (MTS Synergie 200). During the test, the crosshead moved vertically and upwards at speeds of 1 mm/min and 5 mm/min for the PIP and CVI/CVD lattice structure, respectively. Beyond a certain value of displacement, the sample came into contact with the upper aluminum plate at the two nodes adjacent to the strut being tested (Fig. 2.c). A damping rubber layer was inserted at the contact to avoid any early damage of the material. Once the contact was established, the sample remained secured by the holding cage and the pulling load was gradually applied from the nylon yard to the strut, while the crosshead was being translated, until the strut was detached from the structure. The applied load was

simultaneously recorded as a function of the crosshead displacement. These tests were performed on 4 struts of a CVI/CVD lattice structure and 3 struts of a PIP structure (all the struts being located on the outer faces) to obtain an average of the failure load (F_f).

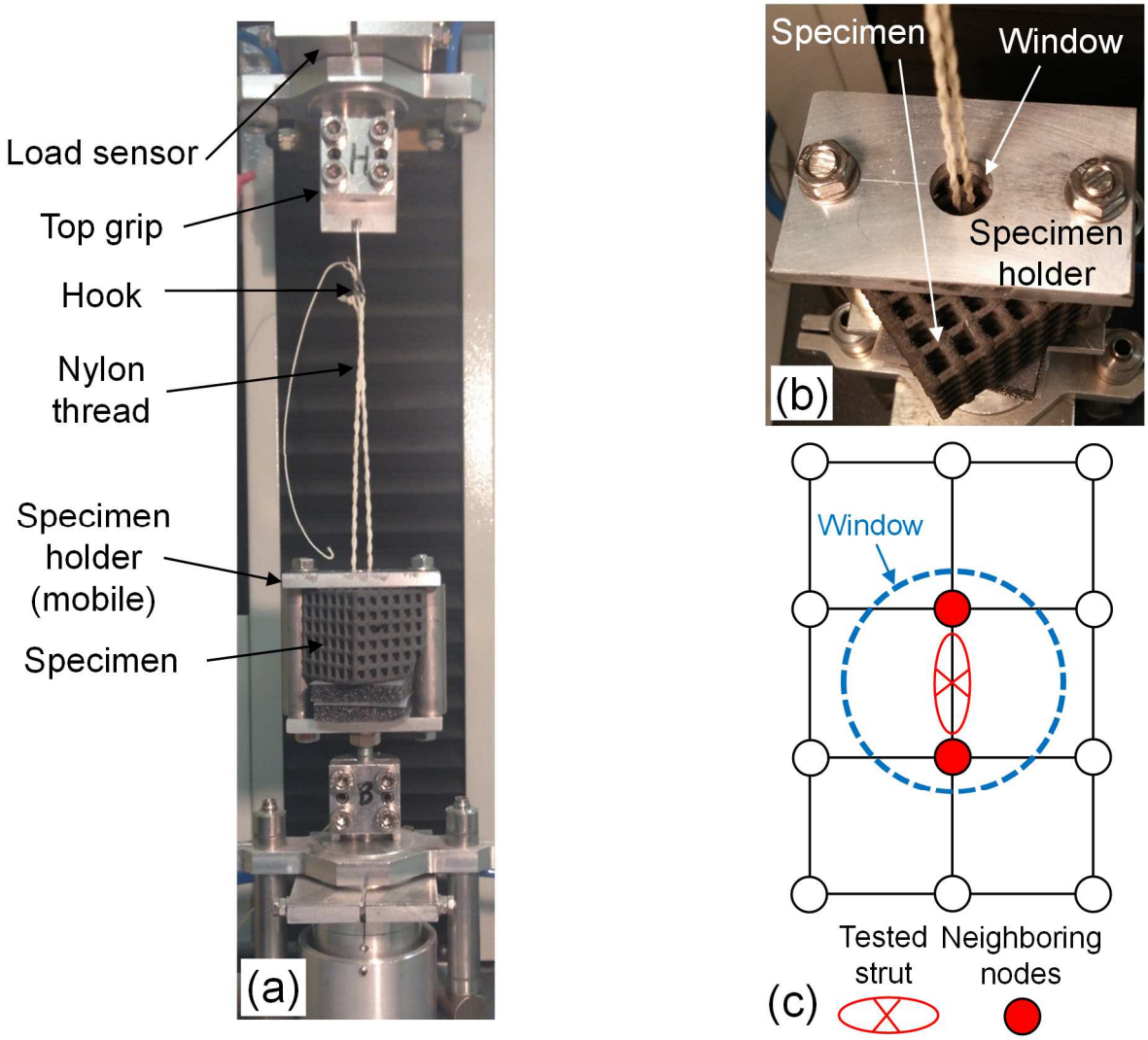

Fig. 2. (a) Global view of the device used for the single strut tearing tests, (b) cellular lattice structure and nylon thread positioning in the specimen holder, (c) schematic showing the tested strut, neighboring nodes and specimen holder window positioning

Thermomechanical analyses (TMA Setsys 2400, from Setaram, France) were performed on PIP and CVI/CVD lattice structures to determine the thermal expansion behavior of the two types of material. A small sample consisting of one half of a cubic cell was cut from a larger specimen due to the size limitation of the TMA system. For a better stability of the sample during testing, a small alumina tab was inserted between the top of the sample and the hemispherical sensor

(SupMat. 4). A negligible compression load of 5×10^{-2} N was applied to avoid creep deformation while ensuring the stability of the sample during the high temperature measurements. The temperature/time program was run under flowing argon and consisted of a slow heating ramp (5 °C/min) up to 1200 °C, a 10 min dwell time at this temperature and a cooling ramp down to room temperature (-5 °C/min). A blank measurement was carried out in exactly the same conditions, but without any sample, to remove the contribution of the surrounding device from the original signal. A high density polycrystalline α-SiC specimen (sintered, 3.16 g.cm^{-3}, from Boostec, France) was analyzed in parallel with the lattice structures for comparison and validation of the measurements [46]. The corrected strain-temperature curve $\varepsilon(T)$ was then obtained as well as the secant coefficient of thermal expansion $\alpha_{se}(T)$, defined with respect to the room temperature T_0 according to Eq. (4).

$$\alpha_{se}(T) = \frac{\varepsilon(T)}{T - T_0} \qquad (4)$$

The optical properties of circular plates, in the PIP and CVD state, were examined at ambient [47] and high temperatures. The reflectivity and transmittivity were measured at ambient temperature using a Perkin Elmer UV/VIS/NIR Lamba 950 spectrophotometer (wavelength range 0.25-2.5 µm) and a Surface Optics Corp. hemispherical directional reflectometer (SOC 100 HDR, wavelength range 1.5-25 µm). The spectral emissivity in the range 0.25-25 µm was deduced from the measurements using the Kirchhoff law. The total solar absorptivity in the range 0.25-2.5 µm and total emissivity in the range 0.25-25 µm, at ambient temperature, were calculated by integration from the spectral emissivity, the solar irradiance and the black body emittance at 300 K, as deduced from the Plank's law. The high temperature optical measurements were carried-out with the experimental set-up MEDIASE installed at the focus of the 1 MW solar furnace of Odeillo [48]. The sample was heated from the front face at increasing temperatures ranging from 1100 K to 1500 K. Its temperature was measured from the rear face with a two-color pyro-reflectometer (at 1.3 and 1.55 µm). The normal spectral emissivity was also measured from the rear face. It is important to mention that the signal was recorded within the limited range of 1.4-14 µm of a CI-Systems SR-5000N spectrometer (the 0.2-1 µm range signal could not be exploited). The high temperature optical properties should therefore be considered with caution. The measurements were calibrated beforehand using a black body. It is also worth mentioning that the samples were kept under air at atmospheric pressure during the high temperature measurements.

The thermal diffusivity of the components of the CVI/CVD lattice structures was measured at the micrometric scale by photoreflectance microscopy, from the cross-section of a polished sample. The photothermal microscope has been described in details in references [49] and [50]. The power-modulated pump beam (2 W, 532 nm, from Coherent Verdi laser) was focused on the surface of the sample with a metallographic microscope. The probe beam was produced by a 20 mW Coherent Sapphire laser (wavelength 488 nm). The amplitude and phase of the photothermal signal was extracted with a 2 MHz-passband lock-in amplifier. The sample was placed on motorized micrometric translation stages to obtain photothermal images or profiles. The phase-shift signal analysis was carried out at variable distance and fixed frequency. The method for thermal diffusivity estimation has been largely described in [49] and [50]. Measurements of SiC-based components are difficult because of the semi-transparency of this material at the pump beam wavelength (532 nm). To circumvent this problem, a 30 nm ± 5 nm thick Pt coating was deposited on the polished sample surface. The areas of the solid parts analyzed were selected after observation under an optical microscope, to ensure that they were homogeneous at the scale of photoreflectance microscopy.

The thermal diffusivity was also determined at the macroscopic scale as a function of temperature up to 1000 °C. In this case the circular plates in both PIP and CVD states were tested by the flash method. The specific device used for the diffusivity measurements is described elsewhere [51]. The tests were performed in air from room temperature to 1000 °C, by increments of 200 °C. The thermal conductivity was deduced from the thermal diffusivity measurements. The specific heat C_p of the two specimens was measured up to 1000 °C by differential scanning calorimetry (DSC 404C from Netzsch). The C_p and diffusivity values as a function of T and the apparent densities were used to calculate the thermal conductivity as a function of temperature.

Thermogravimetric analyses (TGA, Setaram TAG 24) were carried out to assess the oxidation behavior of the ceramics at high temperature and atmospheric pressure in dry air. Four different types of porous materials were submitted to the oxidation tests. The first one, referred to as “SiC-powder”, was the powder used during the binder jetting 3D-printing process. The second and the third type were respectively PIP and CVI/CVD lattice structures. Due to size limitations, a single cubic cell was cut from a larger PIP specimen and tested either as is, or after CVI/CVD (except at the contact with the suspension hook during deposition, the CVI/CVD coating was continuous and undamaged). Finally, the fourth type of material consisted of a CVD rod. In this case one end of the rod was cut after deposition of the CVD coating, exposing the cross-section

to oxidation. Two types of temperature-time program were applied. For the first three materials, the program consisted of a fast (20 °C/min) heating ramp up to 1200 °C, which was maintained during 10 h before cooling down to room temperature (20 °C/min). For the CVD rod, the program consisted of a fast (20 °C/min) heating ramp up to 1200 °C, followed by a dwell time of 50 h and a cooling ramp down to room temperature (20 °C/min). A 4-point bending test was carried out at room temperature on the rod oxidized after TGA.

To simulate the thermal shock and fatigue that can withstand the 3D lattice structures during their use as a solar receiver, a small experimental device was specifically set up to test CVD rods at high temperature (Fig. 3.a).

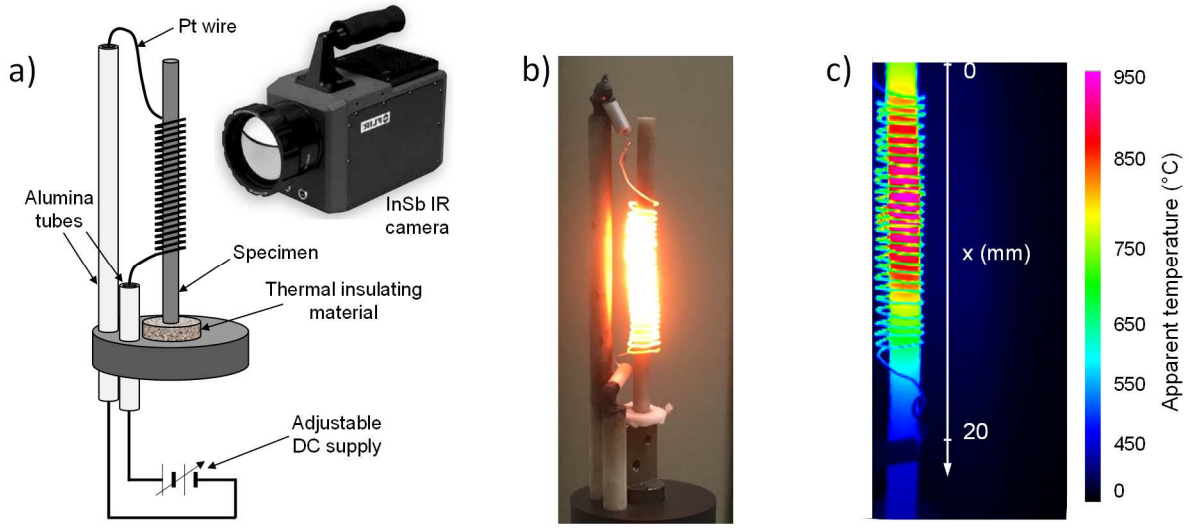

Fig. 3. (a) Schematic of the device used for the thermal shock and fatigue tests in air (b) platinum wire heating during the test of an alumina rod, (c) example of 2D temperature map recorded with the InSb infrared camera

A 0.3 mm platinum wire was coiled to the shape of the rods. The coil (25 mm length, 5 mm in diameter) was connected to an adjustable direct current supply and heated by joule effect in ambient air at temperatures above 1200 °C (Fig. 3.b). The small scale of the specimen and the resistive heating system allowed the fast heating and cooling of the central part of rod. The temperature was acquired by two different ways. An optical bicolor pyrometer (Ircon Mirage) was used for a rapid control of the temperature in the range 700-2000 °C, measured at the center of the rod. The surface analyzed being of a few mm^2, this technique was not able to properly differentiate the local temperature of the platinum wire and the sample. An InSb infrared camera (FLIR SC7000, detection window: 2.5-5.5 µm) was therefore used to record the temperature distribution of the entire rod and Pt wire at high spatial resolution over a range of 300-1500 °C.

Video recordings were performed with the IR camera, from which 2D temperature maps (Fig. 3.c) or axial temperature profiles along the rod were extracted. It should be mentioned that the material emissivity has to be set to a constant value (independent of T) for temperature quantification. The emissivity of SiC was chosen to prioritize the temperature of specimen at the expense of the platinum wire (the emissivity of platinum is as low as ≈ 0.1 against ≈ 0.9 for SiC [52]). Three different annealing tests were performed in ambient air on the CVD rods. The first test consisted in a fast heating of the sample up to approximately 900 °C (the Pt wire being heated up to about 1400 °C) for a period of 90 s, cooling by natural convection down to room temperature for 90 s and a second identical heating and cooling cycle. The supply voltage of the Pt coil was kept constant during the heating period and zero during cooling (neither the temperature of the Pt wire nor the temperature of the sample was regulated). In the second test, another rod specimen was subjected to 70 thermal heating and cooling cycles (as explained above) to analyze the effect of thermal cycling. The third test consisted in heating the sample up to ≈ 900 °C for a longer duration time of 70 min before cooling down. 4-point bending tests were carried out on the annealed specimens resulting from the last two experiments.

3. Results and discussion

3.1. Morphology, structure, microstructure and chemical composition

3.1.1. Surface morphology

Fig. 4. compares successively the surface morphology of the struts of the PIP structure, the same after CVI (referred to as CVI) and the latter after CVD (referred to as CVI/CVD). For the PIP lattice structure, the strut appears extremely rough and porous (Fig. 4.a). After the PIP process, the polymer-derived ceramic (PDC) is intimately mixed with the SiC powder particles. The PDC was found to coat most of the SiC particles. It forms either a rugged and porous material, irregularly distributed, or smooth and fractured blocks of a few tenths of microns, resulting from the polymer shrinkage (Fig. 4.b). These two different types of PDC-based materials probably result from the infiltration of the binder phase and the binder-free inter-grain porosity, respectively. The first step of CVI (with slow deposition kinetics) allows covering all the outer surface, even at the entrance of the open porosity. The high initial roughness is noticeably smoothed out by the uniform coating (Fig. 4.c and Fig. 4.d). The surface of the deposit is either smooth or granular (Fig. 4.d), suggesting a sub-microcrystalline microstructure [36, 53]. The second CVD coating is obviously much thicker as it completely smoothened the struts at the sub-millimeter scale and filled the pores originally located at the surface (Fig. 4.e).

An angular morphology, with small facetted pyramids (Fig. 4.f) typical of microcrystalline SiC, is observed due to the high deposition temperature of 1200 °C.

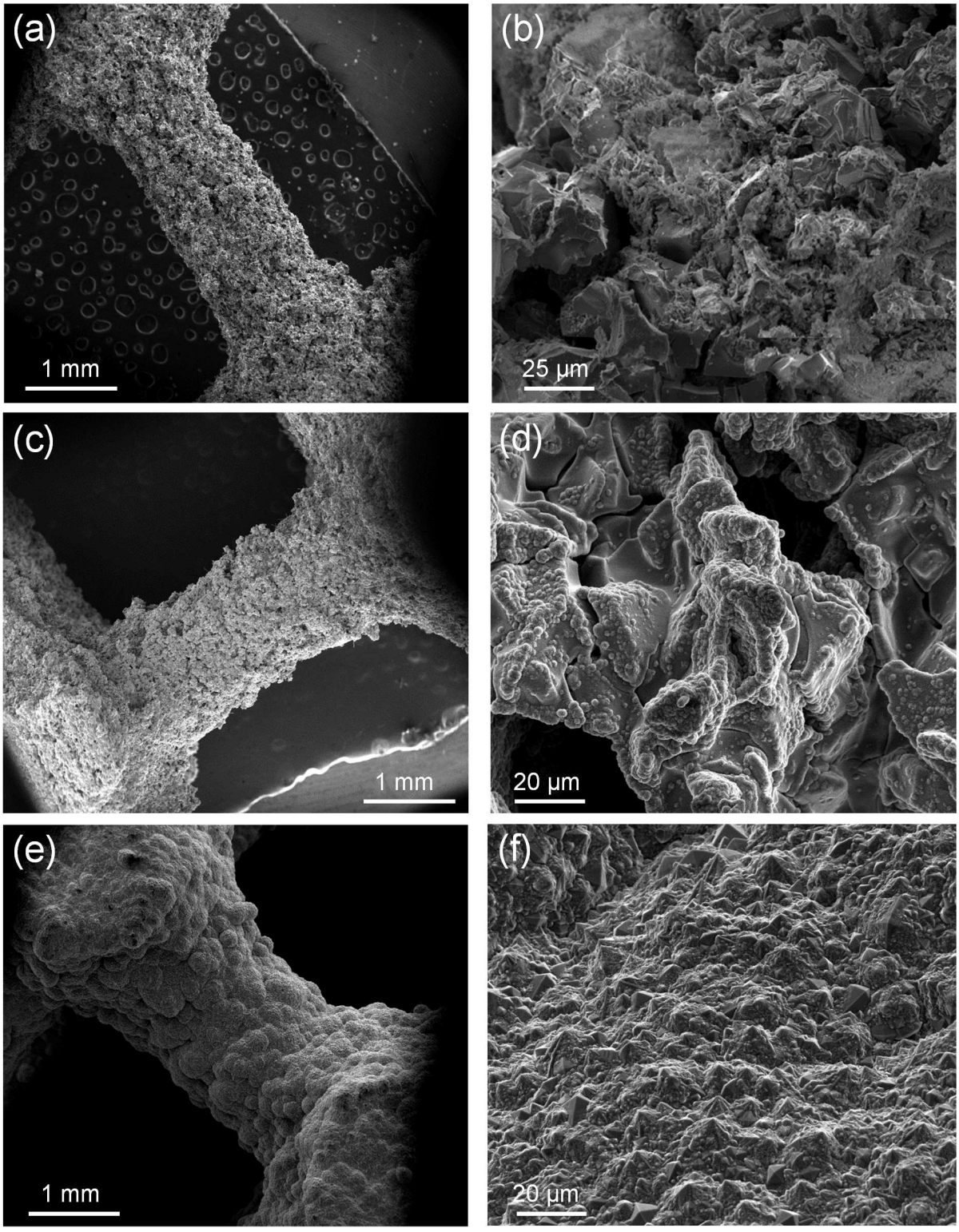

Fig. 4. SEM images (SE mode) of a strut: (a) and (b) as-printed lattice structure, (c) and (d) lattice structure after CVI, (e) and (f) lattice structure after CVI and CVD

3.1.2. Phase composition and microstructure

The different phases and their degree of crystallization in the material at the various stages of the process were analyzed by Raman microspectroscopy (RMS) (Fig. 5), directly from the outer surface, without any preparation of the specimen. For the PIP lattice structures, the spectra recorded from PDC blocs exposed at the surface show only very wide and intense D and G bands at 1350 and 1580 cm^{-1} (Fig. 5.a), which are characteristic of disordered sp^2 carbon [54, 55].

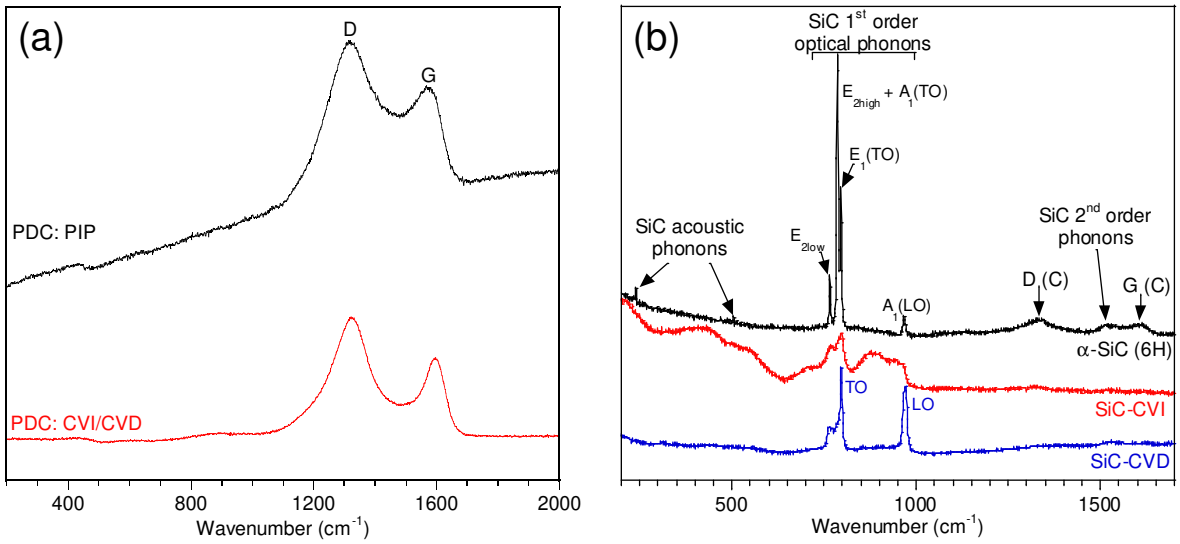

Fig. 5. (a) Raman spectra of the PDC parts in the lattice structures at various stages of the process, (b) Raman spectra of an α-SiC particle, the CVI and the CVD-SiC coating in the lattice structures

This result is in agreement with previous studies showing that the ceramic obtained by pyrolysis of the AHPCS precursor is essentially amorphous for T < 1150 °C [56, 57] and contains free carbon [56, 58]. The Raman spectra from α-SiC particles present at the surface of the PIP structure show weak and narrow peaks at low frequency (< 600 cm^{-1}), which are characteristic of the acoustic phonons of the major α polytypes (see Fig. 5.b, at about 250 cm^{-1} and 500 cm^{-1} for the 6H phase) [59]. The most intense peaks in the spectra correspond to the optical phonons of the α polytypes (6H in the case of Fig. 5.b), i.e. E_1(TO), A_1(TO) and E_2 in the range 770-795 cm^{-1} and E_1(LO) at 970 cm^{-1}. Weak D and G bands are also often observed at high frequency in addition to the second order SiC features, due to the surrounding PDC. The SiC deposit obtained by CVI at 950 °C is poorly crystallized. The SiC Raman features are indeed extremely wide and characteristic of a small grain size and a β (3C) structure with a high density of structural defects such as stacking faults or grain boundaries [60, 61]. The coating is free of sp^2

carbon but the presence of a small excess of amorphous free silicon (visible as a large band centered at 450-500 cm^{-1}) cannot be excluded.

The Raman spectra obtained from the CVD coating, at the surface of the CVI/CVD lattice structure, shows only fine and intense SiC peaks at 796 cm^{-1} and 970 cm^{-1} (Fig. 5.b). These features correspond to a high purity carbon-free and silicon-free coating, consisting of highly crystalline 3C-SiC crystals with a low density of stacking faults.

To complete the phase analysis and examine the microstructure in the bulk, two struts of respectively a CVI (at an intermediate stage) and CVI/CVD lattice structure were cut, polished and examined by optical microscopy (OM) (Fig. 6 and 7) and RMS. The PDC parts are clearly visible in dark grey by OM whereas the α-SiC and CVI-SiC are indistinguishable from each other as they both appear in light grey at the same brightness. The carbon Raman bands recorded from the PDC parts are slightly thinner than after pyrolysis due to the annealing at 1200 °C (Fig. 5.a). The large open porosity left by the porogen material is clearly visible by OM at low magnification for the CVI sample (Fig. 6.a). A CVI-SiC layer of variable thickness is always located at the pore edges (Fig. 6.b-c). The multiple shrinkage cracks in the PDC obviously provided an additional access, on the micrometer scale, to the gases during CVI. The PDC cracks are partially or completely filled with CVI-SiC, the pure SiC material forming a continuous –light grey– network (although they cannot be distinguished, CVI-SiC probably covered also most of the α-SiC phase). Despite some thickness gradient between the surface and the bulk (Fig. 6.b-c), the CVI-SiC coating efficiently filled the finer pores and cracks, ensuring the cohesion between the various SiC-based constituents. In the CVI/CVD sample, the CVD-SiC coating can be easily found as a thick outer layer (90 µm in average) all around the CVI/CVD strut (Fig. 7.a and Fig. 7.b). It is also present far from the surface, due to the high initial surface roughness of the CVI sample (Fig. 7.c). The CVI and the CVD coatings could not be differentiated by OM or by RMS, probably owing to the crystallization of the former during deposition of the latter at 1200 °C and the tight chemical interaction between the two. Yet, the comparison of the CVI and the CVI/CVD samples shows that the CVD coating also reached the core in the open pores left by the binder material (Fig. 7.c). It is only a few micron-thick, even in the largest pores, due to the difficult access of the gases. Some large residual pores (10-100 µm) are indeed left after CVD, but only in the bulk (Fig. 7.a). In the dense areas of the strut, which represents the major part of the material, the three SiC-based constituents are intimately interconnected to each other all across the microstructure (Fig. 7.b).

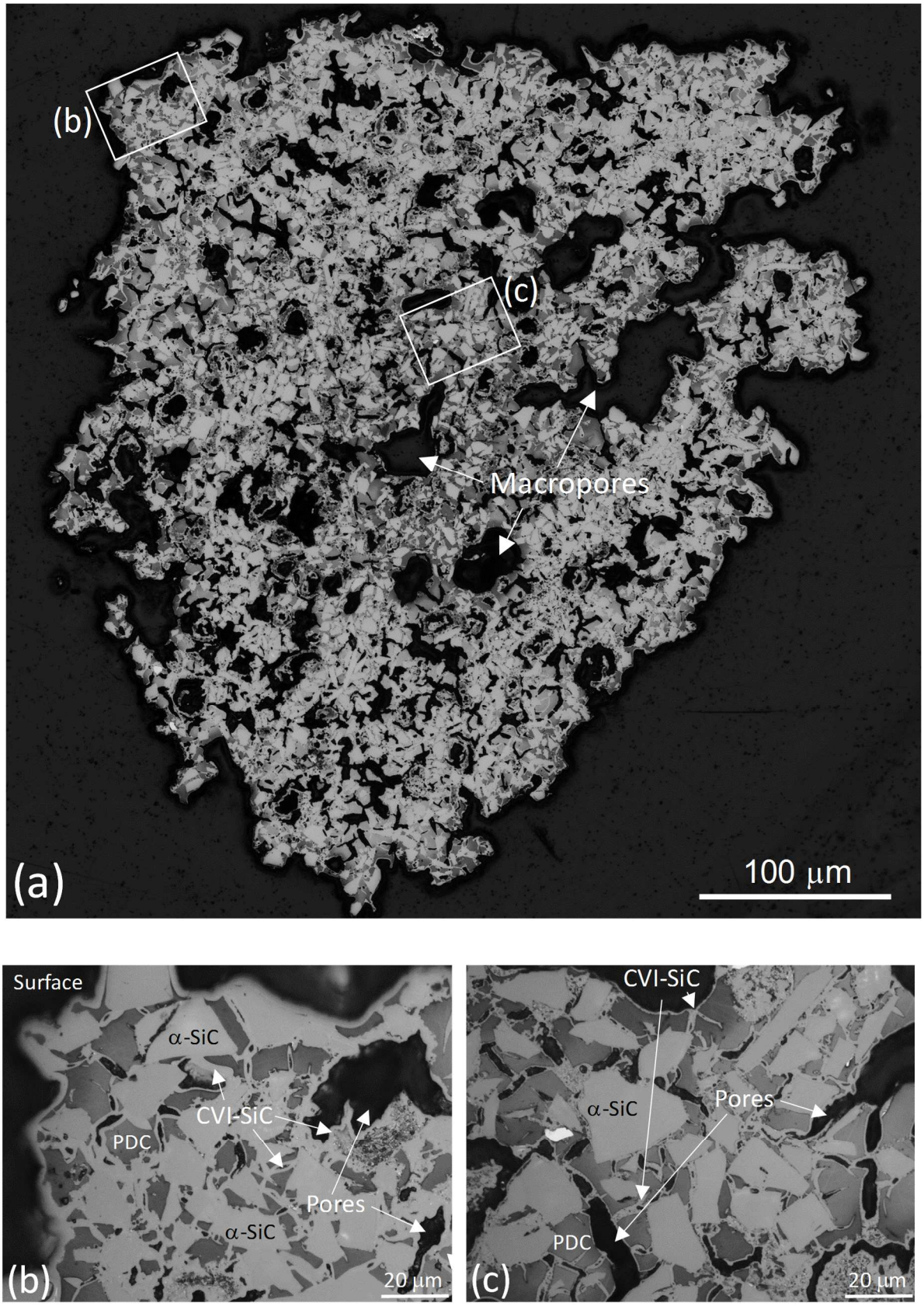

Fig. 6. Strut cross-section of a in a CVI lattice structure: (a) overview, (b) close view near the surface, (c) close view of the core

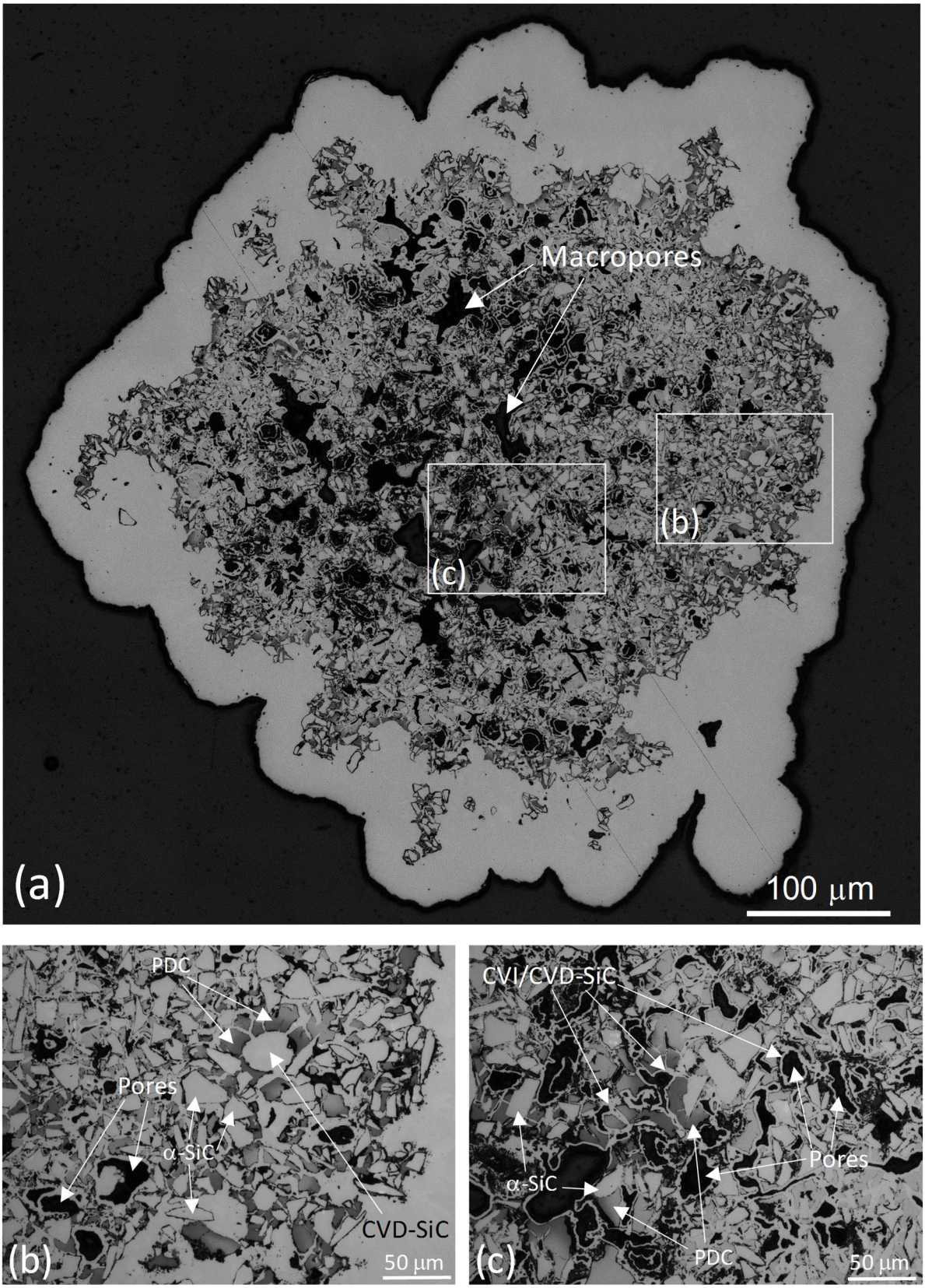

Fig. 7. Strut cross-section of a in a CVI/CVD lattice structure: (a) overview, (b) close view near the surface, (c) close view of the core

The infiltration of the CVI/CVD coating between the α-SiC particles and the PDC blocks (including shrinkage cracks) is effective, even in the center of the strut (Fig. 7.c).

The elemental composition of each component of the CVI/CVD lattice structure as measured by EPMA is presented in Table 2. The composition of the CVI coating is not reported due to uncertainties related to insufficient thicknesses. The results show that the α-SiC particles and the CVD-SiC coating are stoichiometric and oxygen free, with the exception of measurement errors. Conversely, a large excess of carbon (≈ 13 at. %) is found in the PDC as well as a significant amount of oxygen (≈ 9 at. %). The amount of excess carbon is in reasonable agreement with the literature data [56, 58] and is consistent with the Raman analyses revealing strong D and G bands (Fig. 5.a). The crystallinity of the SiC phase in the PDC is indeed limited at 1200 °C [56, 57] (the deposition temperature of the CVD coating), while the Raman scattering efficiency for sp^2-C is ten times higher than for SiC [62]. The high oxygen content can be explained by the fact that the impregnation and the curing step of the AHPCS precursor up to 250 °C were both carried out in ambient air.

The model rods were also examined for comparison with the lattice structures. A cross-section of a rod was examined by OM and X-ray tomography after CVD (SupMat 5). It should be remembered that the diameter of the printed rods (~2.6 mm) was twice as large as that of the struts in the lattice structures (1.3 mm) and that no CVI step was applied on the rods between PIP and CVD. As a result, the SiC coating could not reach the central part of the sample, the infiltration front being limited to a depth of about 500 µm below the initial outer surface. Hence, only the α-SiC powder particles, the PDC blocks and a large residual porosity are observed in the center of the rods.

3.1.3. Density and porous network

The objective of the CVI and the CVD steps is to reinforce the lattice structures by infiltrating the open porosity of the struts and nodes with SiC. The results of both He-pycnometry and Hg-porosimetry show that the densification of the lattice structures first by CVI and finally by CVD is effective (Table 3). Indeed, nearly 40 % of the open porosity of the PIP lattice structure is filled after the intermediate stage and 80 % at the end of the CVD process. The theoretical density of SiC being 3.2 g/cm^3 and porosity being essentially open due to the PDC shrinkage cracks, the $\rho_{\text{true}}^{\text{He}}$ value of 3.0 g/cm^3 for the PIP sample can be explained mostly by the contribution of the PDC (around 2.6 g/cm^3 based on another work [38]). The weight proportion of the α-SiC and PDC in the PIP lattice structure was indeed of approximately 70 and 30 %,

respectively. The decrease of $\rho_{\text{true}}^{\text{He}}$ from 3.0 to 2.8 g/cm^3 after CVI could be attributed to the closing of the small porosities present in the plaster/AHPCS residues. Finally, the re-increase of $\rho_{\text{true}}^{\text{He}}$ after CVD (from 2.8 to 3.0 g/cm^3) is probably related to the infiltration and deposition of the pure and high density CVD-SiC coating in significant amount (it represents 63 wt.% of the final CVI/CVD structure). Such a true density value, however, reveals the presence of residual closed porosity in the final material. On the other hand, the apparent density $\rho_{\text{app}}^{\text{Hg}}$ increases by 40 % after CVI and 100 % after CVD, as a consequence of the proportion of CVI-SiC and CVD-SiC introduced in the material.

In comparison, the model rods are less dense and more porous than the CVI/CVD lattice structures. In agreement with the OM analyses, which showed a poorer infiltration through the core, the open porosity P_{pycno} of the former material is equal to 23 %, i.e. significantly higher than for the latter (13 %).

The pore size distribution of the PIP lattice structure, as measured by Hg-porosimetry, ranges from 0.05 to about 500 µm, with a larger proportion comprised between about 1 and 30 µm (Fig. 8). As expected, the pore size distribution in the CVI sample is narrowed mainly at the small size edge, with pore sizes of 0.5-600 µm. As suggested above, the elimination of the smallest sub-micrometer pores could be related to the infiltration by the CVI coating of the plaster/AHPCS residues. After CVD, the residual porosity in the CVI/CVD lattice structure has vanished, especially in the range 5-50 µm.

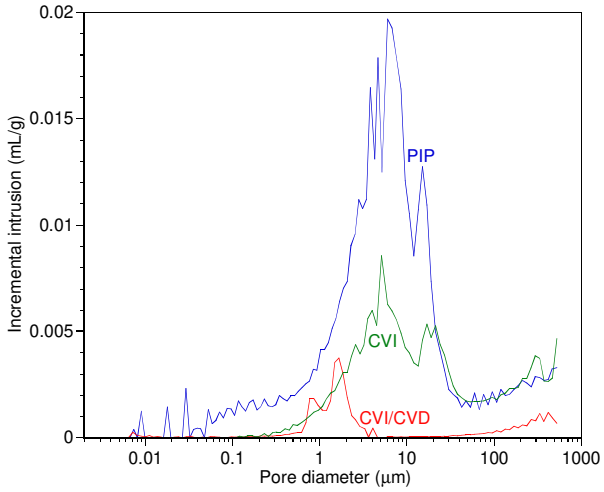

Fig. 8. Pore size distribution in the PIP and CVI/CVD lattice structures, as measured by Hg-porosimetry

In agreement with the OM observations, its consists of a combination of small pores (0.5-5 µm), inaccessible to the reactive gases and large pores (< 50 µm) left by the porogen material. In agreement with the porosity analyses, the BET measurements show that the specific surface area (S_s) is dramatically reduced due to the filling or clogging the finest porosity by the SiC coating. S_s is indeed 1.1 m^2/g in the PIP state, due to the high open microporosity and it drops down to less than 0.3 m^2/g (the limit of quantificantion) for the CVI and CVI/CVD samples.

Non-destructive analyses of the porous network were also carried-out by X-ray tomography. Examples of pictures extracted from the 3D images are presented for the PIP and the CVI/CVD lattice structures in Fig. 9.a to Fig. 9.d and Fig. 10.a to Fig. 10.d, respectively.

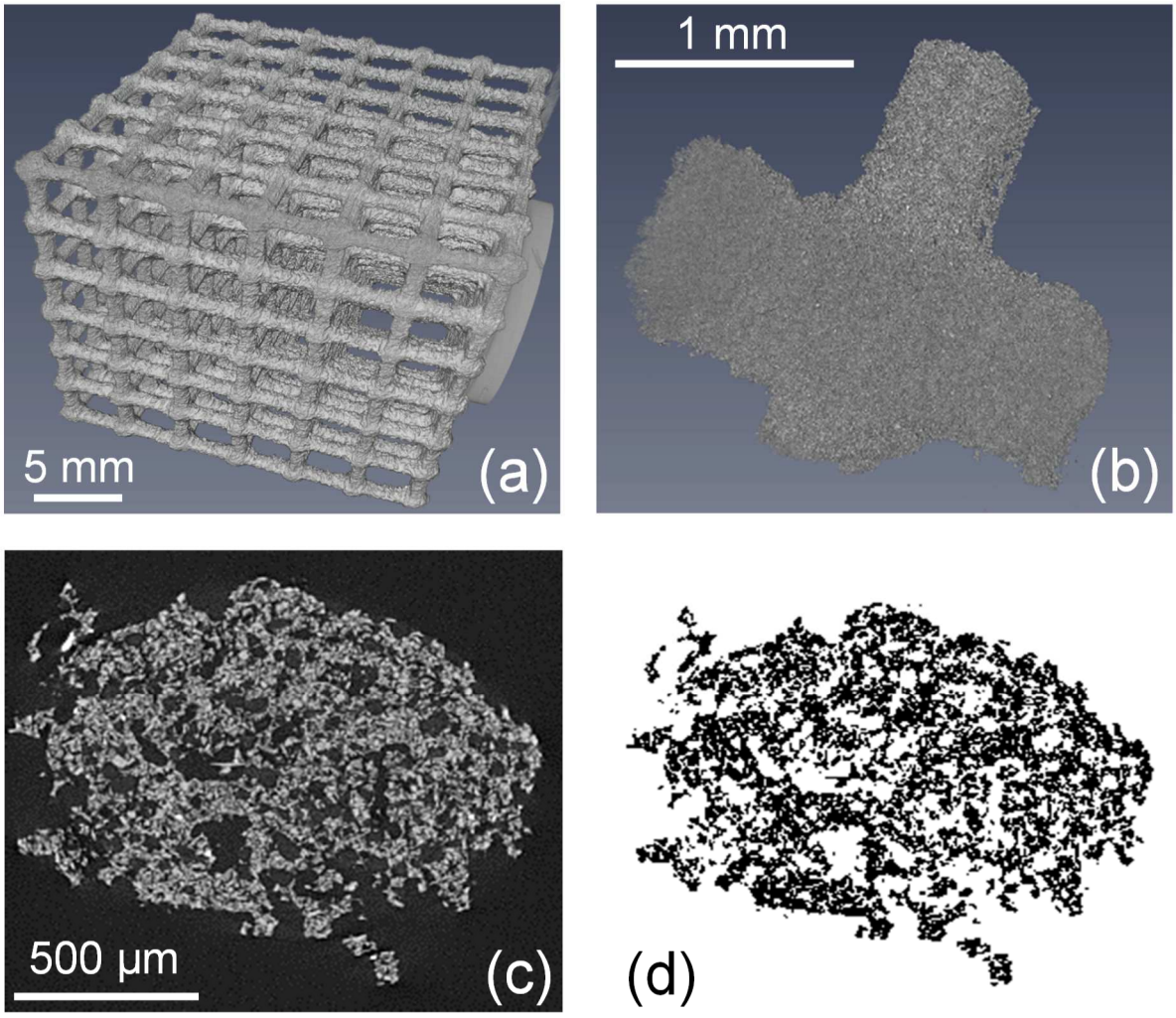

Fig. 9. X-ray tomography images of the PIP lattice structure: (a) overall perspective view obtained at low resolution (23 µm), (b) perspective view at high resolution (2 µm) of a node and its neighboring struts, (c) example of a greyscale image of a strut cross-section, (d) equivalent threshold image

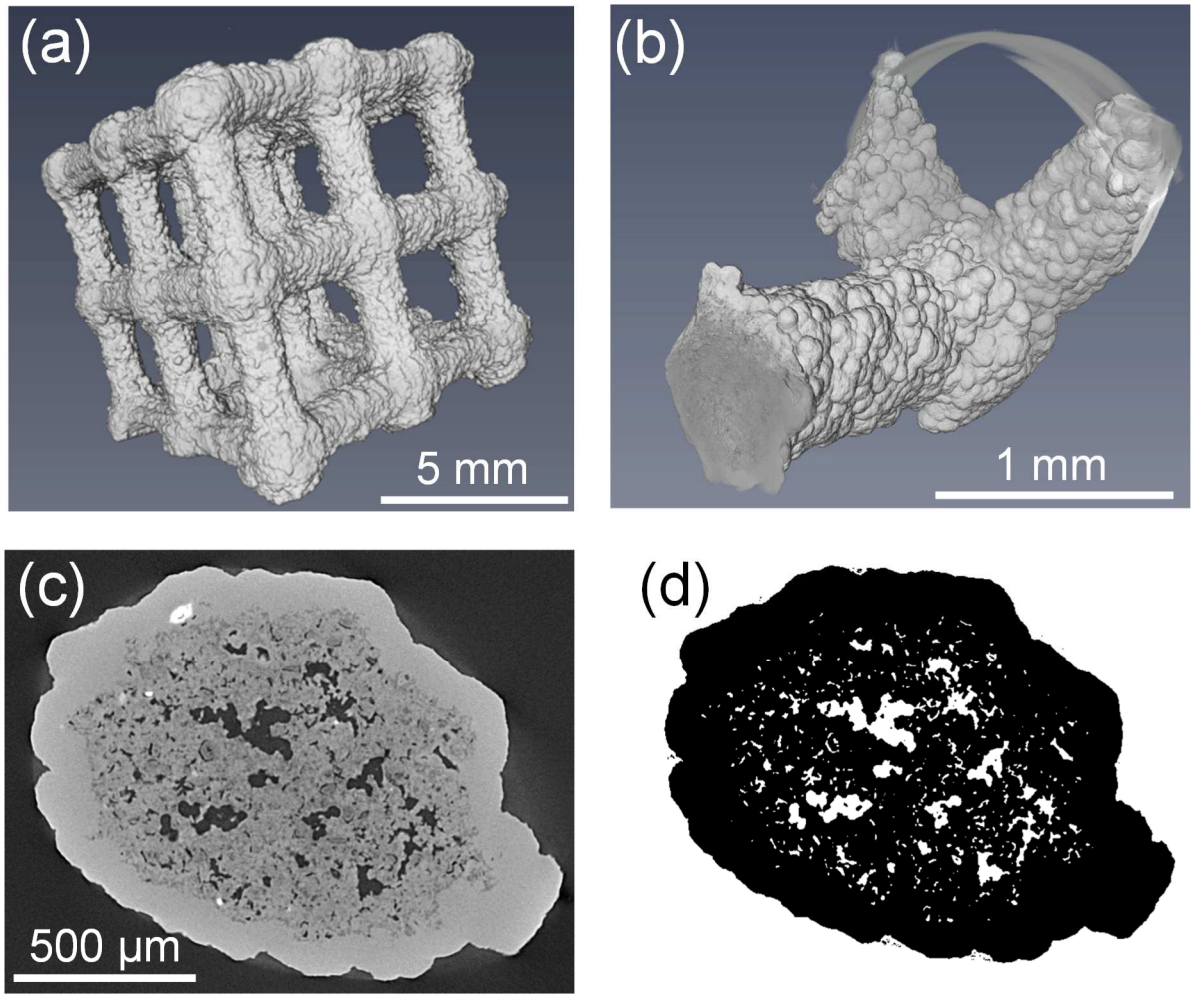

Fig. 10. X-ray tomography images of the CVI/CVD lattice structure: (a) overall perspective view obtained at low resolution (23 µm), (b) perspective view at high resolution (2 µm) of a node and its neighboring struts, (c) example of a greyscale image of a strut cross-section, (d) equivalent threshold image

Overall perspective views of the surface morphologies of the two structures are shown in Fig. 9.a and Fig. 10.a for modeling the total volume of the samples (with an image resolution of 23 µm). Details of a node and struts are given in Fig. 9.b and Fig. 10.b and the cross-section images extracted in the middle of a strut are shown in Fig. 9.c and Fig. 10.c (image resolution: 2 µm). These grayscales images were binarized after thresholding to get Fig. 9.d and Fig. 10.d. The porosity values obtained by image analysis are close to those previously measured by He-pycnometry and Hg-porosimetry (Table 3). The tomographic analyses revealed that the cross-section of the vertical struts (aligned along the printing direction) is circular, as expected from the CAD file, whereas the horizontal struts have an elliptical shape (Fig. 9.c, Fig. 9.d, Fig. 10.c and Fig. 10.d), probably due to some deformation during printing. For the same reason (but this

cannot be seen on Fig. 9 and Fig. 10), the horizontal struts are not perfectly straight. The thick and dense SiC-CVD coating can easily be identified on the tomography images. Its thickness is very homogeneous all around the struts and nodes (Fig. 10.c and Fig. 10.d). The largest porosities are also clearly visible in the bulk of the ligaments. The high level and the multiscale character of the open porosity of the PIP material, evidenced in Fig. 9.c and Fig. 9.d, appear essential for an effective infiltration of the CVI and CVD coating.

3.2. Mechanical properties

The 3D cellular structures were only submitted to pull-out tests to characterize the failure of the single struts. The tests were performed on the PIP, CVI, and CVI/CVD lattice structures, on the upper face of the structures during printing. Examples of damages caused by the tests on the PIP and the CVI/CVD lattice structures are shown in Fig. 11.a and Fig. 11.b, respectively. The struts tested were selected at least one node away from the edges, or from previously damaged nodes, to avoid affecting, as much as possible, the load to failure of neighboring struts. The pull-out loads recorded for the different tested struts of the first PIP specimen are low, of the order of $F_f = 0.8$ ($\pm$ 0.1) N). The failure often propagates to one or several neighboring cells, but usually occurs between nodes. The load at failure is significantly increased after CVI, with an average value of $F_f = 27$ ($\pm$ 2) N. It is still considerably improved for the CVI/CVD specimen, by a factor of about 250 compared to the PIP specimen ($F_f = 200$ ($\pm$ 16) N). The failure mode of the CVI/CVD sample is also different. In this case only the tested struts were detached from the structure. The crack always initiated at the two bottom junctions with the vertical struts underneath. It propagates through the nodes and finally to the top of the neighboring struts (Fig. 11.b). Even if qualitative, such a difference in the failure properties clearly evidences the strengthening of the material due to the infiltration with the CVI and CVD-SiC coating. The reinforcement effect is all the more pronounced as it is the surface of the structure –the most mechanically stressed– that benefits most from the thick CVD coating and therefore from the reduction of roughness, porosity and defect density.

The rods were submitted to several mechanical tests to evaluate the changes in both stiffness and strength of the material at the PIP and CVD stage. Only the CVD rods could be characterized by acoustic analysis, the PIP rods being too brittle and too porous to produce any exploitable signal. The elastic modulus E_{acou} obtained from an average of values for three different rods is equal to 201 ± 12 GPa (Table 4). This value is similar to those for SiSiC lattice

ceramics made by 3D printing and containing 60-80 vol% free silicon [28], but relatively low compared to those reported for pure bulk CVD-SiC coatings, typically in the range 360-450 GPa [63, 34]. It is obviously related to the residual porosity of the material [34] as well as the high surface roughness, which probably leaded to overestimating the geometrical cross-section by micrometer measurements.

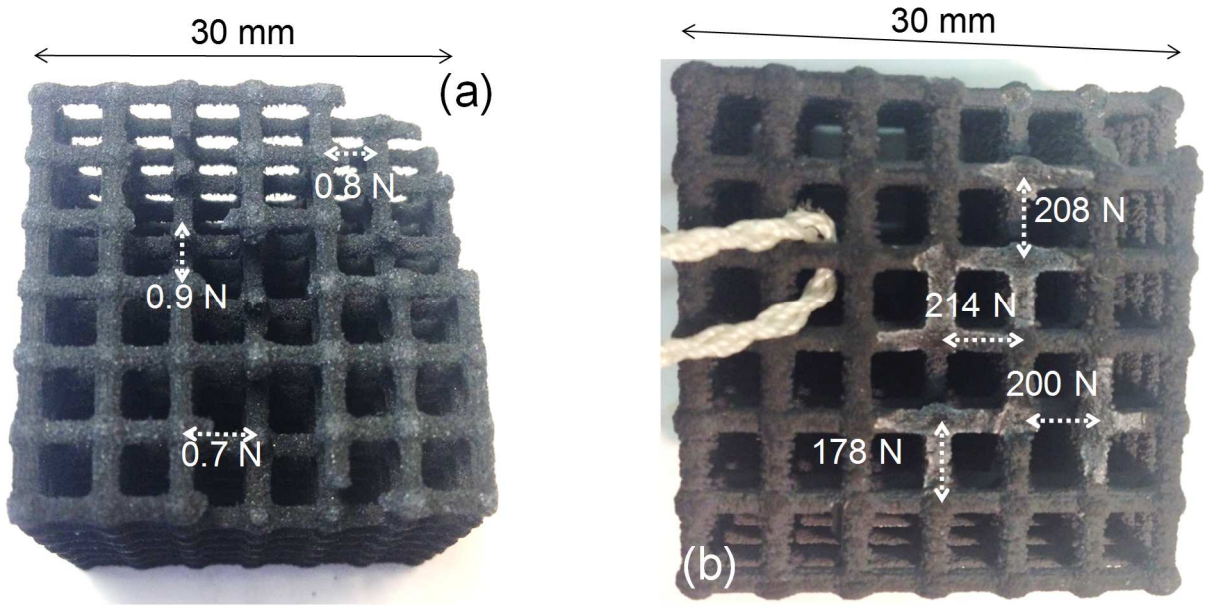

Fig. 11. (a) PIP and (b) CVI/CVD lattice structures after the single strut tearing tests: the locations of tested struts and the corresponding tearing forces are indicated on the pictures

Four-point bending tests were also carried out on the rods to measure the flexural modulus E_{bend} and the failure strength σ_{bend}. Typical load-displacement curves (P-Δ) are plotted in Fig. 12 for the PIP and the CVD specimens (here Δ was measured by image correlation). As a better illustration of the behavior of the material, the maximal stress-strain curve was calculated from the previous data and presented in SupMat 6. These curves are linear-elastic, typical of the brittle behavior of a monolithic ceramic. The mean elastic moduli E_{bend} obtained by image correlation or with the extensometer and the compliance correction are reported in Table 4, as well the failure strength σ_{bend}. Both Δ measurement methods give similar E_{bend} values, validated besides by testing of the reference alumina rod. The number of SiC rods being limited, the Weibull's statistics could not be applied on the distribution of σ_{bend}.

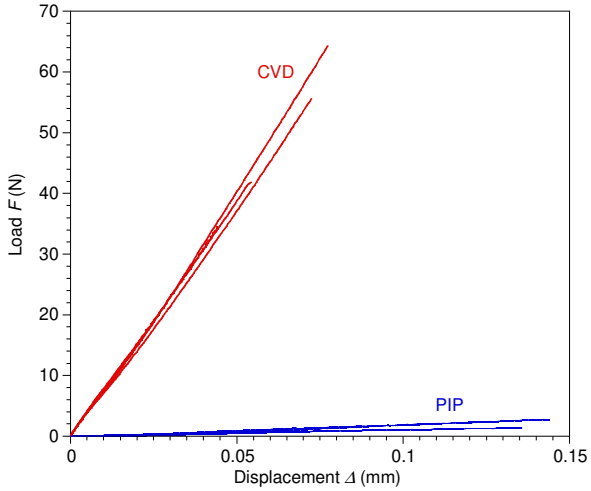

Fig. 12. Load-displacement curves of the PIP and CVD rods recorded during the four-point bending tests

The increase in both E_{bend} and σ_{bend} after CVD clearly reveals the effective strengthening provided by the SiC coating. The vibrational method gives only access to the elastic modulus, but it has the advantage of being non-destructive. E_{acou} and E_{bend} were measured successively on the same specimen and found rather similar. Yet, E_{acou} was generally found higher than E_{bend} (Table 4), probably owing to the very different strain levels applied during the two tests. Some of the rods were not all ideally straight and could not be considered as regular (see section 3.1.2 and 3.1.3). Each specimen had its distinctive properties (mass, dimension, density…), leading to a rather high dispersion of the elastic modulus and, even more due to the flaw distribution, of the failure strength (Table 4). The relative increase of σ_{bend} after the CVD treatment on the rods is not as high as that of F_f, as measured by pull-out tests on the lattice structure. This can be explained by the more efficient SiC infiltration and strengthening of the lattice structures. The strut diameter of lattice structures is indeed 1.3 mm while it is greater than 2.6 mm for the rods. Moreover, the rods were not treated by CVI prior to CVD, so the infiltration of the core was less effective and the SiC coating mostly concentrated near the outer surface. This is probably the reason why the average value of σ_{bend} (≈100 MPa) is somehow limited compared to that for dense SiSiC cellular ceramics tested in similar conditions (up to ≈220 MPa) [28]. σ_{bend} is still considerably higher than the values measured for porous SiC ceramics (<20 MPa), either 3D printed [64] or extruded as honeycombs for a VSR application [6].

3.3. Thermo-physical properties

3.3.1 Thermal expansion

The thermal expansion of the various SiC specimens is compared in Fig. 13: the thermal strain $\varepsilon(T)$ and the secant CTE $\alpha_{se}(T)$ (see Eq. (4)) are presented respectively in Fig. 13.a and Fig. 13.b. $\varepsilon(T)$ and $\alpha_{se}(T)$ were presented rather than the tangent value $\alpha_{ta}(T) = d\varepsilon/dT$ that is more often given in the literature ($\alpha_{se}(T)$ approaches $\alpha_{ta}(T)$ for $T \approx T_0$ whereas it is usually lower than $\alpha_{ta}(T)$ for $T > T_0$). This choice was made for greater clarity of the data ($\varepsilon(T)$ and the reference temperature T_0, for which $\varepsilon(T_0) = 0$, are often omitted) and providing a more direct evaluation of thermal stresses ($\sigma = E\alpha_{se}(T)(T - T_0)$, see section 3.5.) An excellent agreement is found between the values measured from the reference α-SiC specimen and those found in the literature for the same material [46] or other types of pure and dense SiC, whatever the polytype [65]. As expected, the thermal expansion of the CVI/CVD sample is very close to that of the reference α-SiC. Similar measurements were carried out by other authors on 3D printed porous SiC ceramics [64]. The CTE value obtained was unexpectedly high ($(6.87 \pm 0.36) \times 10^{-6}$ K^{-1} in average between 20 and 1000°C, compared to $(4.94 \pm 0.17) \times 10^{-6}$ here for the CVI/CVD specimen) but it was not further discussed. The thermal expansion of the PIP sample is significantly lower than of the CVI/CVD sample, especially at low temperature (Fig. 13.a, Fig. 13.b). Such a particular behavior of the latter probably results from a combination of various effects, including of course the higher contribution of the PDC (which contains free C), but also the high residual porosity and the microstructure itself. The porosity, together with the contrast of the elastic properties, affects indeed the apparent CTE [66]. This effect is likely rendered even more complex by the particular distribution of the different solid constituents and the presence of shrinkage cracks (see section 3.1.2).

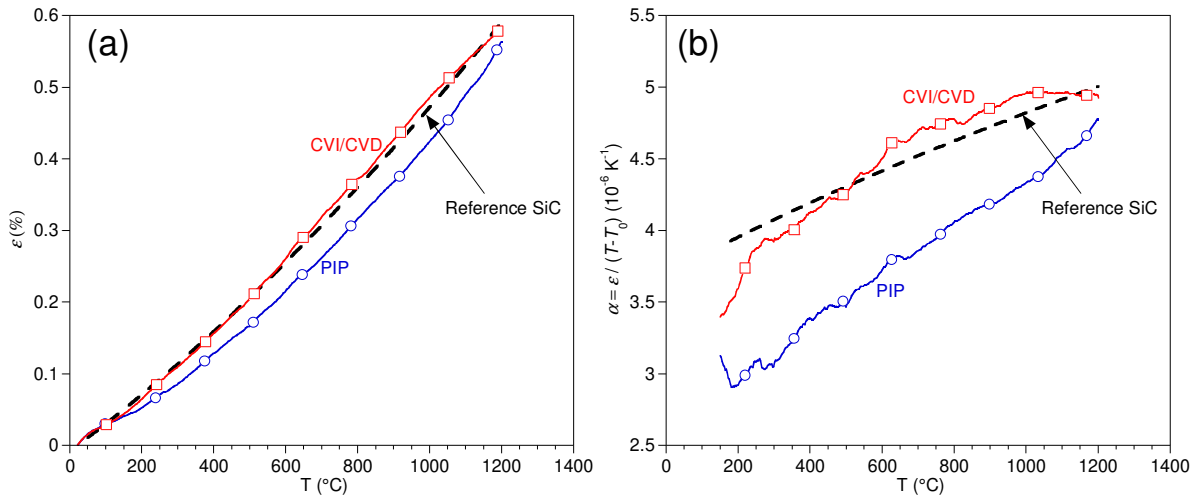

Fig. 13. (a) Thermal strain ε and (b) thermal expansion coefficient α of the PIP and CVI/CVD lattice structures, as measured by thermomechanical analysis

3.3.2 Spectral emissivity and solar selectivity at room and high temperature

The spectral emissivity of the PIP and CVD specimens is compared in Fig. 14. The emissivity value of the PIP material is generally higher in the entire spectral range tested, excepted near the Christiansen wavelength at 9-10 µm. This can be partly explained by the high surface roughness and internal porosity of this specimen leading to multiple reflections and improving light absorption. The different nature of solid, especially the presence of free sp^2 carbon in the PDC, is also probably responsible for such a particular behavior of the PIP specimen.

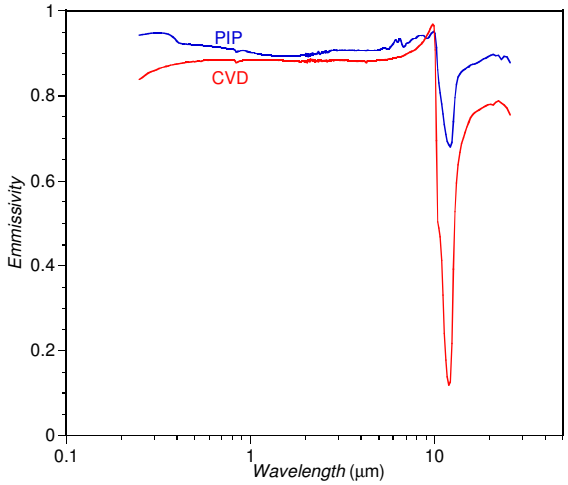

Fig. 14. Spectral emissivity at 300 K of the PIP and CVI/CVD specimens

The weak features appearing at 2-2.8, 4.3 and 5-8 µm were related to the absorption of atmospheric H_2O and CO_2. The strong drop of spectral emissivity in the range 10-14 µm, on the other hand, can be assigned to the high reflectivity band (Reststrahlen band) originating from the excitation of the SiC optical phonons [67] (see the corresponding Raman peaks at 750-1000 cm^{-1} in Fig. 5.b). This band is significantly stronger for the CVD specimen, in accordance with the higher purity and high crystallinity of the CVD-SiC material in comparison with the PDC [68, 69].

The total solar absorptivity, total emissivity and absorptivity/emissivity ratio (a quantification of the solar selectivity) at 300 K are reported in Fig. 15. The PIP specimen has a higher absorptivity and emissivity than the CVD specimen (0.90 and 0.87 versus 0.88 and 0.72, respectively). This is again explained by the higher roughness and internal porosity of the former material, promoting multiple reflection. On the other hand, the absorptivity/emissivity

ratio is improved by the CVD coating (1.22 instead of 1.04), indicative of the better selectivity of the CVD specimen, at least at room temperature.

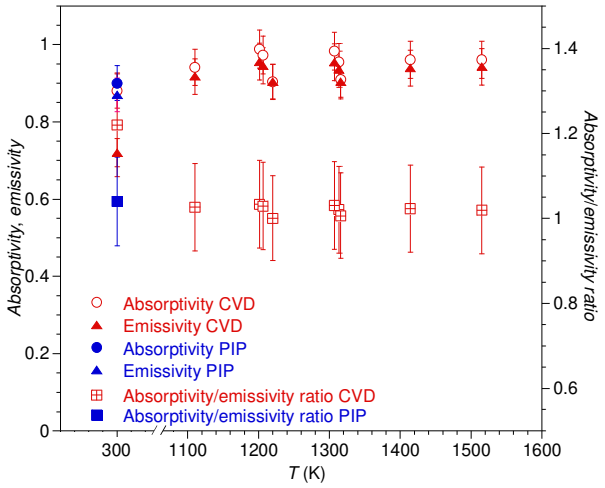

Fig. 15. Optical properties the PIP and CVI/CVD specimens as a function of temperature

The optical properties of the CVD specimen vary from 300 to 1100 K but remain stable between 1100 and 1500 °C (Fig. 15). The average values of the absorptivity and emissivity are respectively 0.95±0.03 and 0.93±0.02 within this range, leading to an absorptivity/emissivity ratio of 1.02±0.01. The emissivity value is higher than for dense sintered SiC specimens tested in air at various pressures (0.71-0.92, see ref. [48]) and even slightly higher for sintered SiC tested in vacuum (0.87-0.92, see ref. [52]). On the other hand, it is very close to that of a C/C-SiC composite coated with a CVD-SiC coating, when tested in vacuum (0.92-0.96, see ref. [70]). Such a behavior suggests that the high emissivity of the CVI/CVD sample is more likely related to its higher roughness (as for the CVD-coated composite) than to surface oxidation [48, 67, 68]. However, these high temperature data are only preliminary and should be updated with a full wavelength integration range (see section 2.2).

3.3.3 Thermal micro-diffusivity

The image recorded with the optical microscope shows the different components of the CVI/CVD material, as well as the spot of the pump beam focused on the surface (Fig. 16). The PDC areas of the specimen were first analyzed. A typical result obtained at an excitation frequency of 150 kHz, after a two-dimensional scanning of the PDC grain shown in Fig. 16, is shown in Fig. 17.a and Fig. 17.b.

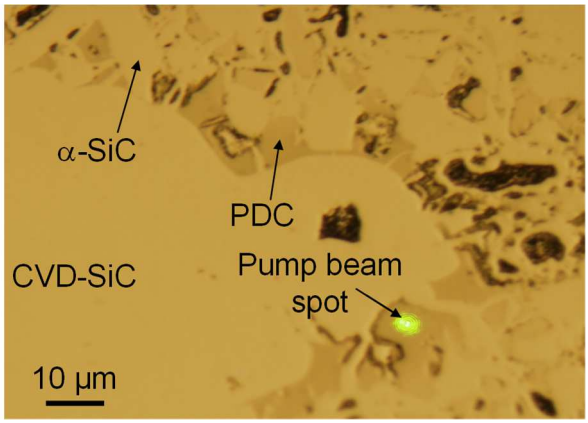

Fig. 16. Optical microscope image of a cross-section of a CVI/CVD lattice structure showing the different SiC-based components and the pump beam spot focused on a PDC part. The darkest zones correspond to pores, brown regions to PDC areas and lightest zones to α-SiC particles and the CVD-SiC coating

The PDC zone investigated does not exhibit any preferred direction of heat transfer. The isolines of the attenuation and phase signals appear indeed circular, i.e. characteristic of an apparent thermally isotropic behavior, as expected for such a highly disordered material.

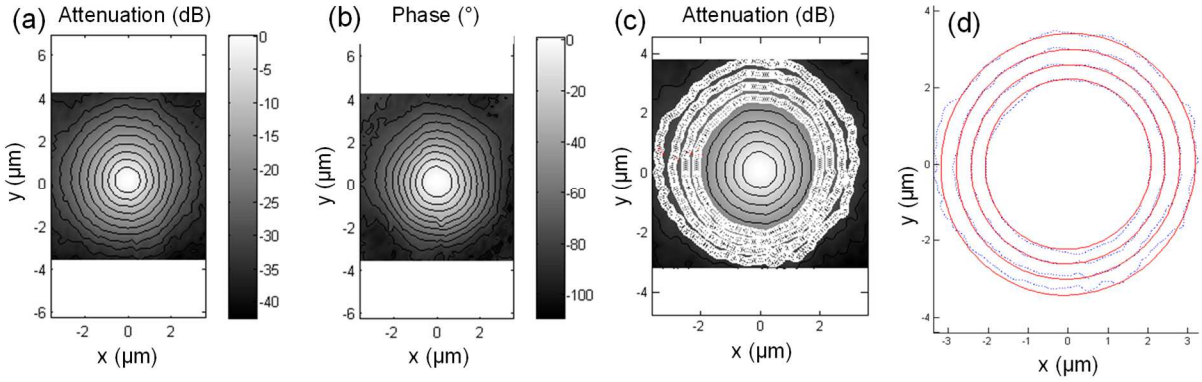

Fig. 17. Thermal micro-diffusivity measurements on a PDC part: (a) attenuation, (b) phase shift 2D mappings recorded at 20°C and a frequency of 150 kHz, (c) and (d) isoamplitude lines fit obtained. The thermal anisotropy factor deduced is equal to 1.02

A thermal anisotropy factor as low as 1.02 was indeed deduced from of the ellipticity degree of the isoamplitude lines (i.e. the square root of the former) through a best fit procedure (Fig. 17.c and Fig. 17.d). Such a thermally isotropic behavior considerably simplified the analysis: measurements could thus be restricted to the acquisition of a one-dimensional radial profile of the thermal signal along any direction, as shown Fig. 18.a and Fig. 18.b.

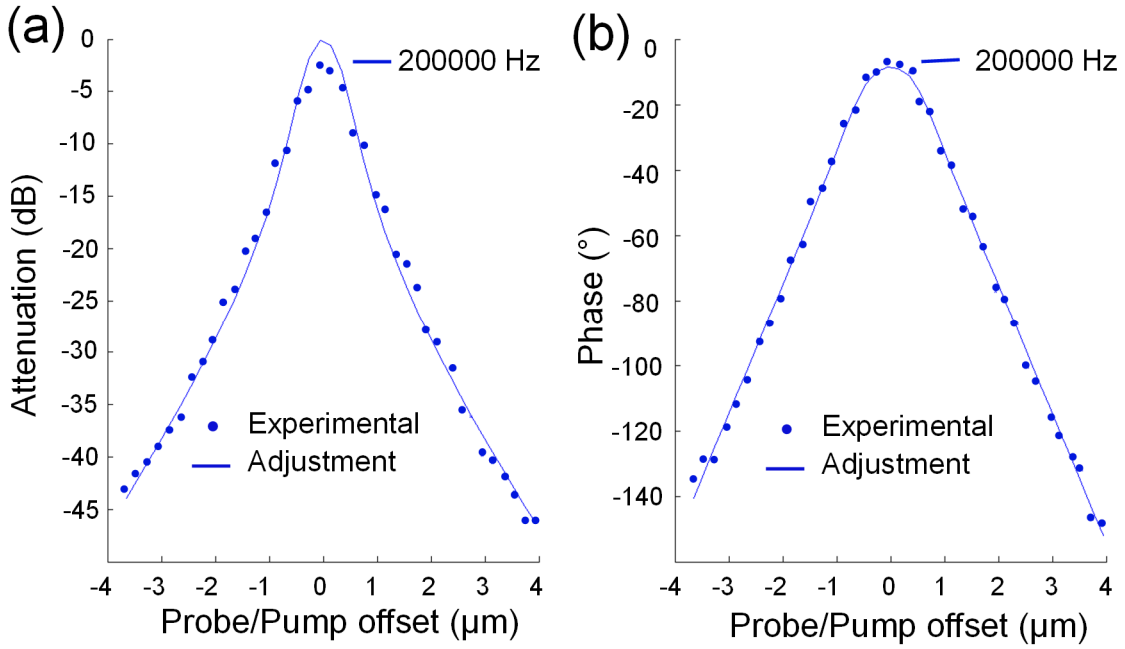

Fig. 18. Thermal micro-diffusivity measurements on a PDC part: (a) attenuation and (b) phase shift 1D profiles recorded at 20°C and 200 kHz, with related least square adjustments

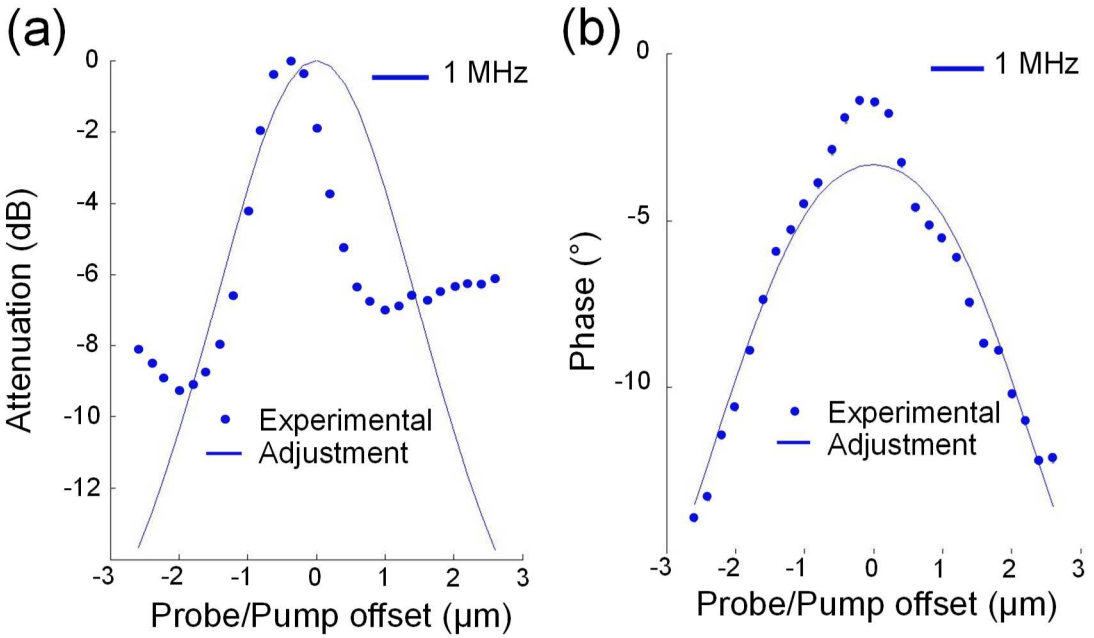

Fig. 19. Thermal micro-diffusivity measurements on CVD-SiC: (a) attenuation and (b) phase shift profiles recorded at 20°C and 1 MHz, with related least square adjustments

The thermal diffusivity was then estimated through a complete Levenberg-Marquart procedure using the best set of coefficients (dimension of laser beams, thermal diffusivities of the substrate and coating, ratio of the thermal effusivities of the substrate and the coating). The statistical

processing of a series of measurements at different places of the specimen led to an average value of the thermal diffusivity of the PDC of $(2.1 \pm 0.4) \times 10^{-6}$ m^2/s at 20 °C. The determination of the thermal diffusivity of the CVD-SiC (though assumed to be thermally isotropic) was much more complicated. The thermal signal was indeed weak and noisy. The attenuation and the phase shift were particularly low, even at high frequencies (up to 1 MHz), denoting a very diffusive material as shown by the profiles obtained at 1 MHz (Fig. 19.a and Fig. 19.b). The least square adjustment is poor and large discrepancies appear due to the very weak signal. Several profiles recorded at frequencies ranging from 1.0 to 1.2 MHz led to a thermal diffusivity value of $(4.1 \pm 2.3) \times 10^{-4}$ m^2/s. Despite the high uncertainty, this result confirms the very diffusive nature of the CVD-SiC. The analysis of the α-SiC grains was not attempted because of their small size, irregular shape and expected high thermal diffusivity.

The macroscopic thermal diffusivity (as measured by the flash method from circular plates) of the PIP and CVD specimens is plotted as a function of the temperature in Fig. 20.a.

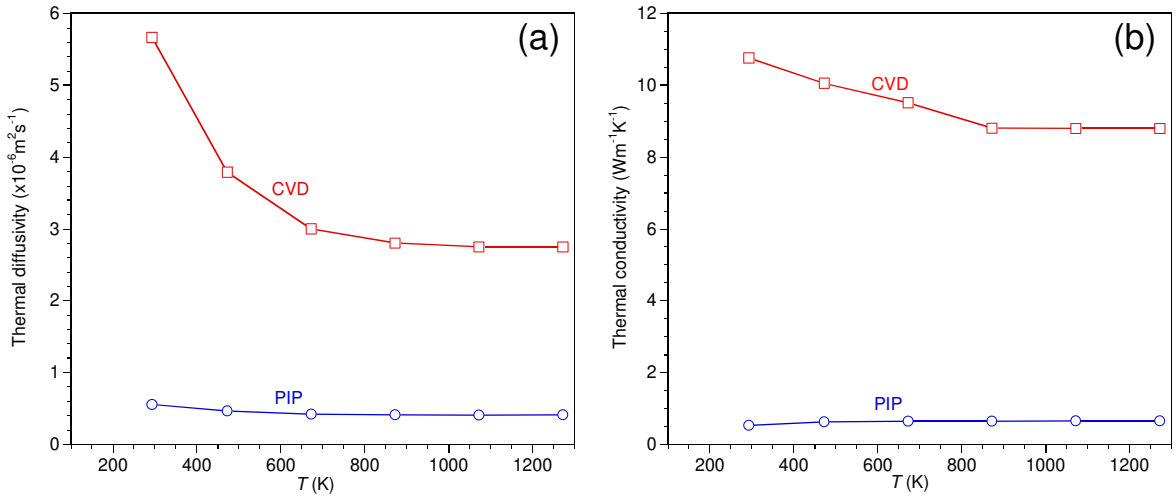

Fig. 20. Thermal diffusivity (a) and thermal conductivity (b) of the PIP and CVI/CVD specimens as a function of temperature

For the PIP specimen, it is equal to 5.55×10^{-7} m^2s^{-1} at 300 K and rapidly decreases down to 4.08×10^{-7} m^2s^{-1} at 873 K, before stabilizing up to 1273 K. The thermal dependence is similar after the CVD step, but the level is more than one order of magnitude higher, i.e. 5.67×10^{-6} m^2s^{-1} at 300 K and 2.80×10^{-6} m^2s^{-1} at 873 K. The macroscopic value for the CVD material at room temperature is comprised between those of the constituents evaluated at the microscale ($2.1 \times 10^{-6} < 5.7 \times 10^{-6} < 4.1 \times 10^{-4}$). This result indicates that the residual porosity does not affect diffusivity too much and that the interfaces between the solid phases are of good quality.

The thermal conductivities of the two materials, as deduced from the diffusivities, densities (see Table 3) and C_p measurements (see SupMat 7), are plotted versus temperature in Fig. 20.b. The conductivity of the PIP specimen increases slightly with T, but remains lower than 1 $Wm^{-1}K^{-1}$ up to 1273 K. This behavior is probably resulting from the high porosity promoting heat transfer through radiation at high temperature. The CVD specimen is significantly more conductive at room temperature (10 $Wm^{-1}K^{-1}$) and its conductivity strongly decreases when T increases, as expected for pure, dense and monolithic SiC [34].

3.4. Oxidation resistance

The relative weight variations ($\Delta m/m_0$) in dry air at 1200 °C were recorded as a function of time up to 10 h for the PIP, CVI/CVD lattice structures, as well as the pure α-SiC powder used for 3D printing (Fig. 21.a). For the PIP lattice structure, the first weight loss observed in the range T = 50-100 °C (t = 0.2 h) corresponds to the elimination of moisture adsorbed at the surface of the sample ($S_s \approx 1$ m^2/g). The second weight decrease occurring between 400 and 650 °C (t = 0.5-0.7 h) is likely due to the oxidation of the free carbon phase present in the PDC, the oxygen access and reaction being favored by the high open porosity and specific surface. The reversal of the curve around 800 °C and the following parabolic weight gain observed along the isothermal plateau at T = 1200 °C result respectively from the terminating gasification of the accessible free carbon phase and the increase of the passive oxidation kinetics of the SiC particles and the PDC. A very similar behavior was observed for the oxidation of SiC honeycombs of high porosity and containing residues of free carbon [6]. The passive oxidation regime, as opposed to the active regime [71], is expected at moderate temperature in dry atmosphere, at high O_2 partial pressure [72, 73, 74], conditions that were typically encountered during the TGA tests. The silica scale formed in these environments is dense and protective. The oxidation kinetics, followed by the silica layer thickness measurements or *in situ* TGA, is therefore expected to obey a parabolic law due to the limitation by the O_2 solid-state diffusion through the SiO_2 layer [72, 73, 74]. The linear evolution as a function of time of the square of the weight gain relative to passive oxidation only (i.e. corrected for the initial weight loss due to the free carbon oxidation), indeed clearly evidence the parabolic oxidation regime of both the α-SiC powder and the PIP lattice structure (Fig. 21.b). The higher slope observed for the latter specimen can be assigned to its higher specific surface (≈ +20 %, from the TGA curves), probably due to the fragmented shape of the PDC blocks (see section 3.1.1). The weight variation is comparatively very limited for CVI/CVD lattice structure (Fig. 21.a). Such a better apparent stability is related to the substantial decrease of the specific surface after CVI/CVD,

as already suggested by the BET analyses (see section 3.1.3). A very similar result was noticed when comparing the oxidation of highly porous re-crystallized SiC and fully dense silicon-infiltrated SiC (SiSiC) [6]. Here, instead of liquid silicon, the thick CVD coating of pure SiC eventually clogged the major part of the open microporosity, leading to the drop of the specific surface and thus of the progress of oxidation. The TGA curve of the specimen is presented separately in Fig. 21.c to better appraise the weight change versus time. The weight loss due to the elimination of free carbon is observed up to about 5.5 h (the small hump at the end of the heating ramp was not assigned: it might be due to an artifact). It is followed by a weight gain, the passive oxidation of SiC starting to prevail over the gasification of free carbon.

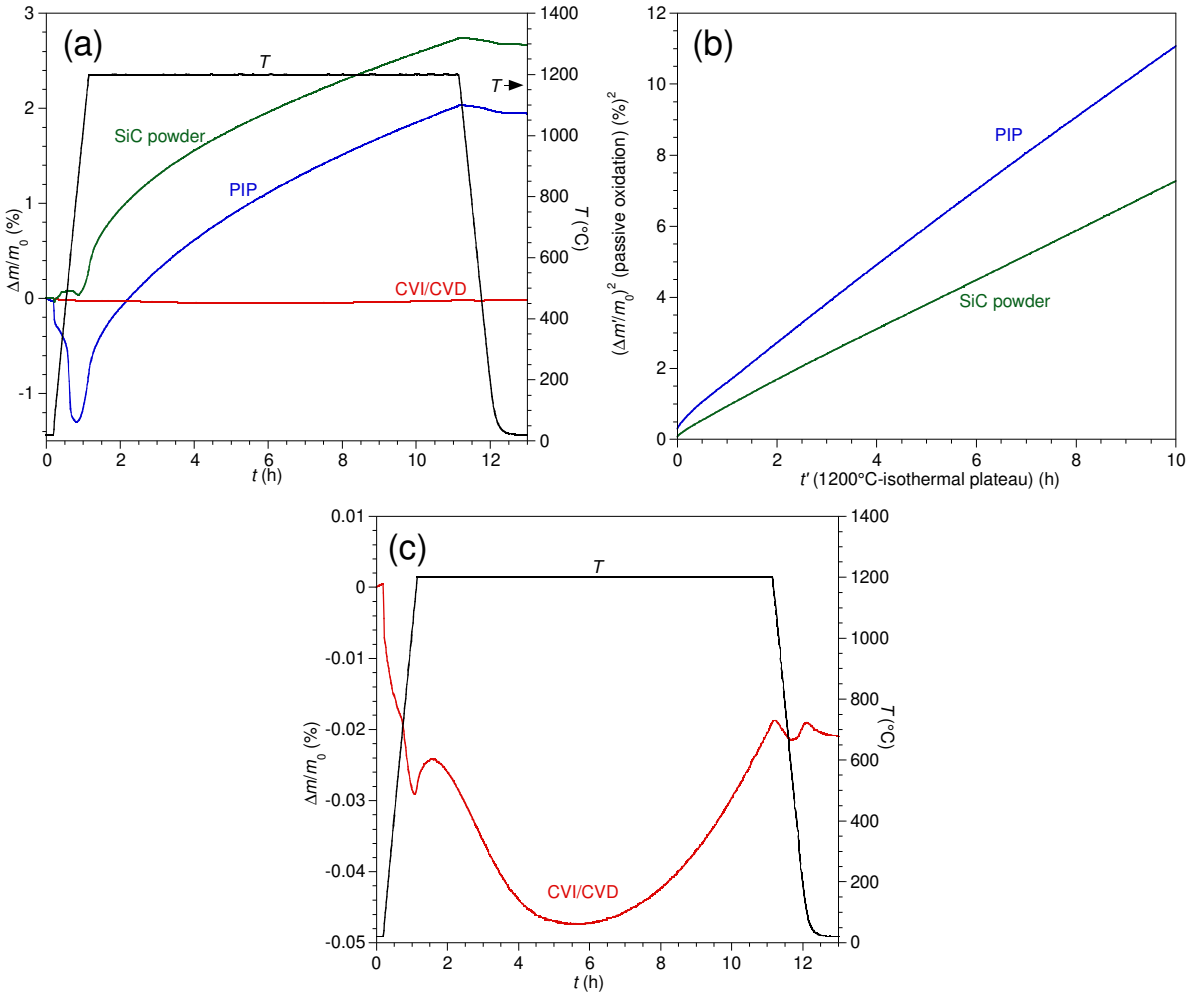

Fig. 21. (a) Relative weight change in dry air as a function of time recorded for the reference α-SiC powder, the PIP lattice structure and the CVI/CVD lattice structure. (b) Square of the relative weight change as a function of time recorded for the α-SiC powder and the PIP lattice structure, during the isothermal plateau at 1200 °C. (c) Relative weight change in dry air as a function of time recorded for the CVI/CVD lattice structure (closer view of the data presented in Fig. 21.a)

The same TGA curve reversal was observed for the PIP structure but for a significantly shorter duration. Most of the PDC domains being covered by the CVI and CVD coatings, the low amount of free carbon still exposed to oxidation is hardly accessible to O_2. SEM-EDS analyses were performed from the outer surface and cross-sections of the two lattice structures. As expected, traces of superficial oxidation were found from both the outer surface and the interior of the PIP specimen (not shown), either on the α-SiC or PDC particles. For the CVI/CVD lattice structure, the oxidation is only concentrated on the outer surface: SEM-EDS analyses showed no sign of oxidation within the CVI/CVD structure. An iridescence phenomenon (not shown) indicates the thickness of the SiO_2 scale is submicrometric.

The TGA and SEM-EDS investigations showed that the PIP structure is prone to oxidation due to its high specific surface and the presence of the free carbon-rich PDC. On the other hand, the CVI/CVD coating effectively suppressed oxidation by (1) reducing the overall specific surface (and so the probability to interact with O_2), (2) increasing the proportion of pure SiC (with respect to the carbon-rich PDC) and (3) reducing the O_2 access to the PDC with a tight CVI/CVD-SiC layer.

A TGA test was also carried out on a CVD rod in the same conditions as for the lattice structures (1200 °C in dry air), but for a duration time of 50 h. The TGA curve also reveals a minimum due to a transition between a loss and a gain of weight, at an intermediate time between that for the PIP and the CVI/CVD specimens (Fig. 22).

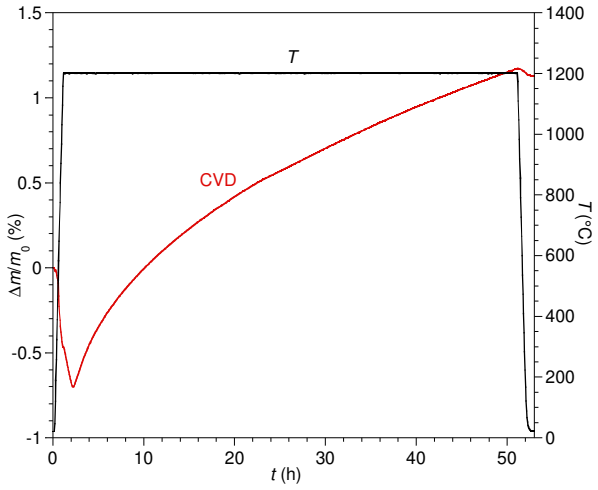

Fig. 22. Relative weight change in dry air as a function of time for a CVD rod

This result should be related to the microstructure observations above (see section 3.1.2) illustrating that the thick CVD-SiC coating did not cover the α-SiC and PDC domains -and thus

did not clogg the open microporosity- as efficiently as for the lattice structures. The tested rod specimen was submitted to a 4-point bending test to examine if the 1200 °C/50 h oxidation treatment induced any weakening of the material. The σ_{bend} and E_{bend} values measured from the CVD rod after TGA are respectively ≈ 20 and ≈ 10 % lower than the original values, but they still remain within the dispersion ranges (Table 4, Table 5). From this preliminary test, it can be concluded that no significant damage was generated by the 1200 °C/50 h treatment, at least on the specimen tested.

3.5. Thermal shock and fatigue in air

The objective of this basic and preliminary test was to evaluate, at the scale of a single strut, the effects, on the integrity of the specimen, of thermal cycling as endured by a volumetric solar receiver during its use. More precisely, the room temperature failure strength of rod specimens was evaluated after a certain number of cycles of fast heating and cooling (respectively at about 900 °C and room temperature) and compared to the original value. This test is of course not fully appropriate to evaluate the thermal stress resistance (TSR) of the lattice structure itself. The ends of the tested rods were indeed not constrained as in real structure, so no longitudinal stresses were generated due to the temperature change. The rods were mainly loaded radially during the test, which is of course much less severe considering, as will be shown below, their small diameter and relatively high thermal conductivity. The aim was not either to precisely evaluate the thermal fatigue resistance (TFR) of the material. Such a study would have required much more tests at different numbers of cycles. The test result, i.e. the residual failure strength, provided the sample has not spontaneously failed during thermal cycling, rather reflects the development of cracks or defects upon thermal cycling under the combined effects of thermal stresses and oxidation.

If one focusses specifically on thermal stresses, one can refer to the work of Kingery and Hasselman [22, 75, 76] respectively on the thermoelastic (through the description of TSR parameters) [22, 75] and strain energy approaches [76]. For instance, in the most severe case of an externally constrained cylinder submitted to ideal surface heat transfer, the maximum admissible temperature decrease ΔT without failure can be simply assessed by Eq. (5):

$$\Delta T = \frac{\sigma_f}{\alpha E} \qquad (5)$$

where σ_f, α and E are respectively the tensile failure strength (assumed to be lower than the compressive strength), the CTE and the Young's modulus. On the other hand, in case of slow surface heat transfer compared to solid heat conduction, the expression of the maximum admissible ΔT involves also the Poisson ration ν, the thermal conductivity of the solid K, the convection heat transfer coefficient h and a geometrical parameter, here, the radius of the rod b [76], as shown by Eq. (6):

$$\Delta T \approx 5\frac{\sigma_f(1-\upsilon)K}{\alpha E b h} \qquad (6)$$

A value of ΔT of about 150 °C can thus be easily deduced from Eq. (5) and compared to the value for any other constitutive material. The value of the parameter h is needed to determine ΔT under the second assumption. Although some numerical values were reported for different heat transfer conditions [22], it is difficult to appraise which one is appropriate in the current case. Yet, the benefit of high K and low b values in the material and geometry selection is obvious from Eq. (6). Although numerous methods have been used to assess the TSR of refractory materials [77], the measurement of the residual flexural strength after thermal cycling is of course one of the reference tests. Hasselman's strain energy theory, based on crack propagation, describes the decrease of the fracture stress as a function of ΔT [76]. Even closer to the current case, residual flexural tests have been used to characterize the thermal behavior of SiC-based ceramics for solar receivers [78].

As explained in section 2.2, the first thermal test applied to the CVD rod consisted in two thermal cycles in air. The spatial and temporal temperature distribution was examined in a first step with the IR Camera. From the 2D image video recordings (Fig. 3.c), the temperature profile along the rod axis at a given time within the first temperature dwell can be plotted (Fig. 23). The sharp downwards peaks along the main parabolic profile correspond to the platinum coils, appearing apparently colder than the CVD rods due to their lower emissivity. The hottest parts of the CVD rod and the Pt coils were identified on the IR image and the temperature was recorded versus time during the two thermal cycles after assigning each material its proper emissivity (Fig. 24).

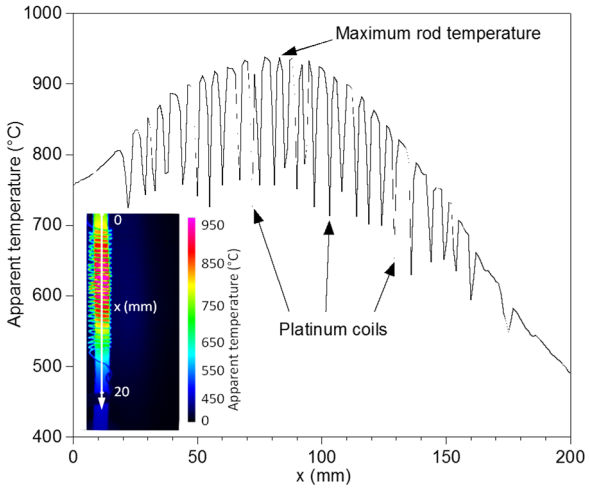

Fig. 23. Thermal shock and fatigue tests in air: apparent temperature profile along the CVD rod and the heating Pt coil, as extracted from 2D temperature mapping obtained with the IR Camera (see inset)

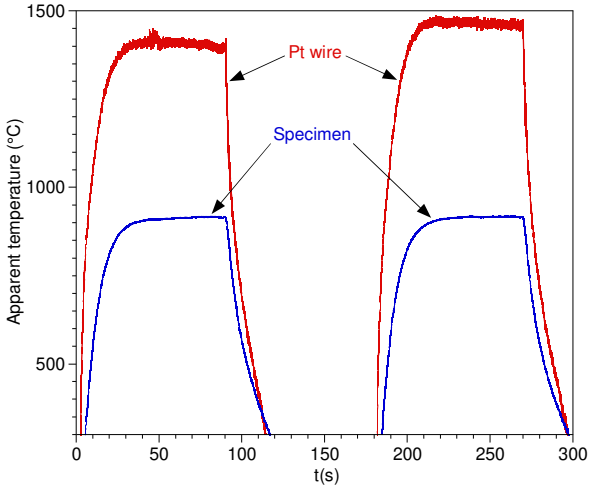

Fig. 24. Thermal shock and fatigue tests in air: temperature changes as a function of time, as recorded from the CVD rod and the Pt coil during thermal cycling

The maximum temperature of the Pt coils approaches 1450 °C whereas that of the CVD rod is only 915°C (±1°C during the last 40 s). In the 300-915-300 °C temperature range, the average heating and cooling rates of the CVD rod are respectively ≈ 25°C/s and ≈ -20 °C/s (65°C/s and -50 °C/s in peak values), i.e. faster than those imposed on volumetric solar receivers in service [79]. Such a heating rate was not high enough, however, to raise thermal stresses within the rod to the point of failure. None of the three tests (two cycles, 70 cycles or a single 70 min cycle) caused the specimens to rupture.

The flexural failure stresses and moduli of the specimens resulting from the last two test were evaluated (Table 5) and compared to the values for the as-processed CVD specimen (Table 4).

Although only one specimen of each kind was tested, most of the values obtained were found within or beyond the uncertainty ranges of the as-processed CVD rods (Table 4). The σ_{bend} value found for the single 70 min cycle, in particular, falls slightly beyond this range. This is probably not a result of the annealing treatment itself, but rather of an exceptionally high apparent density or low defect concentration in this specific pristine specimen. On the other hand, the bending modulus of the sample after 70 short cycles is significantly lower than expected in the initial state. Such a decrease in stiffness, combined with a slightly lower failure stress, might be a consequence of the propagation of pre-existing multiple cracks during the accumulation thermal shocks [76].

Instead of this preliminary thermal shock procedure, a more realistic test would consist in producing (or cancelling) a longitudinal thermal gradient along a constrained rod in a tensile testing device, or a single strut in the 3D lattice structure itself, and measure (or calculate) the resulting tensile or compressive stresses versus time. Such a test remains a challenge as the more relevant case would be a local cooling along an initial hot isothermal structure, to generate more detrimental tensile stresses.

3. Conclusion

SiC-based macroporous open-cell ceramics have been synthesized for use as a volumetric receiver in thermodynamic solar power plants. The millimeter-scale open macroporosity required for the application was generated by CAD before 3D printing. Green α-SiC lattice structures with such a given geometry were then prepared by binder jetting (BJP). The strengthening of the solid part was subsequently achieved by polymer infiltration and pyrolysis (PIP) and chemical vapor deposition (CVD). One original aspect of the process was the creation of a multiscale porosity within the solid prior to the CVD step, to promote the reactive gas infiltration and thus the deposition of CVD-SiC. The porosity at the micrometer scale was essentially related to the compactness of the α-SiC grains and the shrinkage cracks in the polymer-derived ceramic (PDC) formed during pyrolysis. The intermediate macroporosity, in the range 10-100 µm, was set up by using plaster as binder during printing, in the form of a few large agglomerates, and removing it by acid dissolution between the PIP and the CVD steps. To simplify the determination of the various solid part properties, rod-like specimens were also prepared according to a similar procedure.

The second key step in the process, which provides the structures with most of their ultimate properties, is the deposition of pure and dense SiC using a CH_3SiCl_3/H_2 gas mixture. It was divided in two stages in the case of the lattice structures, with (i) a first infiltration of the porous network (at both microscale and macroscale) to the core of the solid struts forming the lattice structure (CVI) and (ii) the deposition of a thick outerlayer (CVD). The various components of the final ceramic microstructure are the starting α-SiC particles, the PDC (containing nanocrystalline β-SiC, excess O and free C), and the CVI and CVD-SiC coatings, both polycrystalline and pure, the latter including coarser microcrystalline β-SiC due to the higher deposition temperature. The microstructure of the lattice structures reveals a high densification level of the pores at the micrometer scale with the CVI/CVD coating. It is almost ideal near the surface and still high in the core, thanks to the combination of initial macro- and microscale open porosity. Only the macropores resulting from the plaster aggregates remain in the bulk of the strut. Thus, for the lattice structures, from the PIP to the CVD stage, the apparent density of the solid part is raised by 100 % while the open porosity is reduced by almost 80 %.

Most of the properties relevant for application as volumetric solar receiver have been examined. The mechanical and thermal properties, the oxidation and thermal shock/fatigue resistance were assessed either directly from the lattice structure struts or from the rods, at the different stages of the processing route. As expected, the dense microcrystalline CVD-SiC coating greatly improves almost all properties. From the PIP to the CVD step, the load to failure of the lattice structure struts is improved by a factor of 250, while the CTE increases of only 12% at 1000 °C. The thermal diffusivity of CVD-SiC is about 200 times higher than that of PDC, resulting in a macroscopic diffusivity (respectively conductivity) of the CVD specimen that is ≈10 (resp. 20) times higher than that of the PIP material. The pure and tight CVI/CVD coating improves considerably the oxidation resistance of the material. The high specific surface and the free carbon-rich PDC make the PIP material sensitive to oxidation. In contrast, the CVI/CVD lattice structures are extremely stable in air up 1200 °C, due to the closure of the open porosity, the reduction of the specific surface and, of course, the excellent oxidation resistance of the β-SiC coating itself.

The thermal shock and fatigue resistance in air result from a complex combination of physical and chemical effects. The lattice structures in solar receivers are not intended to play a real structural function. Damage is thus expected to arise mainly from a combination of oxidation (or corrosion) and thermal stresses. To limit the latter effect, high failure strength and low CTE and elastic modulus are in any case desirable. In the event of poor surface heat transfer, a small

characteristic size (here the diameter of the ligaments) and a high level of thermal conductivity have the effect of reducing temperature gradients and thus thermal stresses. These requirements lead to a good compromise for the CVI/CVD lattice structures. The pure and dense CVD-SiC rim near the strut surface, where stress concentrations may develop, is in favor of a high oxidation resistance and a high strength. The residual porosity in core, on the other hand, limits the stiffness: the elastic modulus of the rod is indeed less than half the theoretical value for dense SiC. The thermal fatigue tests combine repeated thermal shocks and a cumulated oxidation time. In agreement with the preceding oxidation and thermal shock tests, which have been considered separately, the fatigue tests did not reveal cracks in the CVD-SiC coating, traces of oxidation in the core or decrease of failure strength.

The processing route that has been developed gathers several advantages compared to routes based exclusively on PIP, pressureless or reactive sintering. The binder jetting allows the synthesis of large objects with a great variety of 3D structures (fully virtual or derived from real objects), provided the cell struts or walls are thick enough to be printed ($\approx$ 1 mm). Neither template nor specific tooling is required for shaping the green 3D structure. As for sintering, the CVI/CVD process performed at the industrial scale authorizes the simultaneous treatment of large and numerous objects with minimum handling and risk of breakage. At the end of the process, the most part of the material consists of high purity and high crystallinity SiC (of both α and β types), guarantying a high failure strength, thermal conductivity, creep, oxidation and corrosion resistance. Yet, it is difficult to know how much the residual porosity in the strut core affects the mechanical and thermal properties of the lattice structure and how it would eventually affect the behavior of the solar receiver in service. The thermal stress field in the cellular structure and its efficiency as a volumetric solar receiver can be assessed numerically from the basic properties of the solid and the simulation of all thermal exchanges (radiation, convection and conduction). The degradation rate and the lifetime, on the other end, need to be assessed by a sufficient number of realistic and long term tests.

Acknowledgments

This work was supported by the French Alternative Energies and Atomic Energy Commission (CEA) through a PhD grant to A. B. The authors are grateful to B. Humez, L. Lapuyade, G. Couégnat and O. Caty from LCTS, and M. Lahaye from PLACAMAT, for the mechanical tests,

Hg-porosimetry analyses, finite element calculation, X-ray tomography measurement and Castaing microprobe analyses respectively.

References

[**1**] S. Alexopoulos, B. Hoffschmidt, Advances in solar tower technology, Wiley Interdisciplinary Reviews: Int. J. Energy Environ. 6 (2017) e217. http://dx.doi.org/10.1002/wene.217

[**2**] O. Behar, A. Khellaf, K. Mohammedi, A review of studies on central receiver solar thermal power plants, Renewable Sustainable Energy Rev. 23 (2013) 12-39. https://doi.org/10.1016/j.rser.2013.02.017

[**3**] C.K. Ho, B.D. Iverson, Review of high-temperature central receiver designs for concentrating solar power, Renewable Sustainable Energy Rev. 29 (2014) 835-846. https://doi.org/10.1016/j.rser.2013.08.099

[**4**] A.L. Ávila-Marin, Volumetric receivers in Solar Thermal Power Plants with Central Receiver System technology: a review, Sol. Energy 85 (2011) 891-910. https://doi.org/10.1016/j.solener.2011.02.002

[5] D.G. Morris, A. López-Delgado, I. Padilla, M.A. Muñoz-Morris, Selection of high temperature materials for concentrated solar power systems: Property maps and experiments, Sol. Energy 112 (2015) 246-258. https://doi.org/10.1016/j.solener.2014.09.050

[6] C.C. Agrafiotis, I. Mavroidis, A.G. Konstandopoulos, B. Hoffschmidt, P. Stobbe, M. Romero, V. Fernandez-Quero, Evaluation of porous silicon carbide monolithic honeycombs as volumetric receivers/collectors of concentrated solar radiation, Sol. Energy Mater. Sol. Cells 91 (2007) 474-488. https://doi.org/10.1016/j.solmat.2006.10.021

[7] T. Fend, High porosity materials as volumetric receivers for solar energetics, Opt. Applicata 40 (2010) 271-284. http://www.if.pwr.wroc.pl/~optappl/article.php?lp=788

[8] Z. Wu, C. Caliot, F. Bai, G. Flamant, Z. Wang, J. Zhang, C. Tian, Experimental and numerical studies of the pressure drop in ceramic foams for volumetric solar receiver

applications, Appl. Energy 87 (2010) 504-513. http://dx.doi.org/10.1016/j.apenergy.2009.08.009

[**9**] T. Fend, B. Hoffschmidt, R. Pitz-Paal, O. Reutter, P. Rietbrock, Porous materials as open volumetric solar receivers: Experimental determination of thermophysical and heat transfer properties, Energy 29 (2004) 823-833. https://doi.org/10.1016/S0360-5442(03)00188-9

[**10**] T. Fend, R. Pitz-Paal, O. Reutter, J Bauer, B. Hoffschmidt, Two novel high-porosity materials as volumetric receivers for concentrated solar radiation, Sol. Energy Mater. Sol. Cells 84 (2004) 291-304. https://doi.org/10.1016/j.solmat.2004.01.039

[**11**] S. Mey-Cloutier, C. Caliot, A. Kribus, Y. Gray, G. Flamant, Experimental study of ceramic foams used as high temperature volumetric solar absorber, Sol. Energy 136 (2016) 226-235. https://doi.org/10.1016/j.solener.2016.06.066

[**12**] A. Ortona, E. Rezaei, Modeling the Properties of Cellular Ceramics: From Foams to Lattices and Back to Foams (conference paper), CIMTEC 2014 13th Ceramics Congress, Montecatini, Italy, Advances in Science and Technology. 91 (2014) 70-78. https://doi.org/10.4028/www.scientific.net/AST.91.70

[**13**] M. Romero-Alvarez, E. Zarza, Concentrating solar thermal power, in: Handboook of Energy Efficiency and Renewable Energy, Chapter 21, F. Kreith and Y. Goswami eds., CRC Press Taylor & Francis Group, Boca Raton, Florida, 2007, pp. 1-98.

[**14**] Z. Chen, Z. Li, J. Li, C. Liu, C. Lao, Y. Fu, C. Liu, Y. Li, P. Wang, Y. He, 3D printing of ceramics: A review, J. Eur. Ceram. Soc. 39 (2019) 661-687. https://doi.org/10.1016/j.jeurceramsoc.2018.11.013

[**15**] U. Lakshminarayan, S. Ogrydiziak, H. Marcus, Selective laser sintering of ceramic materials, 1990 International Solid Freeform Fabrication Symposium, (1990). https://sffsymposium.engr.utexas.edu/Manuscripts/1990/1990-03-Lakshiminarayan.pdf

[**16**] S. Danforth, Fused deposition of ceramics: a new technique for the rapid fabrication of ceramic components, Mater. Technol. 10 (1995) 144–146. https://doi.org/10.1080/10667857.1995.11752614

[**17**] M.L. Griffith, J.W. Halloran, Freeform fabrication of ceramics via stereolithography,

J. Eur. Ceram. Soc. 79 (1996) 2601-2608. https://doi.org/10.1111/j.1151-2916.1996.tb09022.x

[**18**] E. Sachs, M. Cima, P. Williams, D. Brancazio, J. Cornie, Three dimensional printing: rapid tooling and prototypes directly from a CAD model, J. Eng. Indu. 114 (1992) 481-488. https://doi.org/10.1115/1.2900701

[**19**] J Cesarano III, R Segalman, P Calvert, Robocasting provides moldless fabrication from slurry deposition, Cer. Industry 148 (1998) 94-102.

[20] A. Zocca, P. Colombo, C.M. Gomes, J. Gunster, Additive Manufacturing of Ceramics: Issues, Potentialities, and Opportunitie, J. Am. Ceram. Soc. 98 (2015) 1983-2001. http://dx.doi.org/10.1111/jace.13700

[21] T. Chartier, A. Badev, Rapid Prototyping of Ceramics, Handbook of Advanced Ceramics, Second Edition, chap. 6.5, S. Somiya and M. Kaneko eds., 2013, pp. 489-524.

[22] W.D. Kingery, Factors affecting thermal stress resistance of ceramic materials, J. Am. Ceram. Soc. 38 (1955) 3-15. https://doi.org/10.1111/j.1151-2916.1955.tb14545.x

[**23**] C. D'Angelo, A. Ortona, Cellular ceramics produced by replication: a digital approach, Adv. Eng. Mater. 14 (2012) 1104-1109. http://dx.doi.org/10.1002/adem.201100350

[24] S. Gianella, D. Gaia, A. Ortona, High temperature applications of Si-SiC cellular ceramics, Adv. Eng. Mater. 14 (2012) 1074-1081. https://doi.org/10.1002/adem.201200012

[**25**] A. Ortona, T. Fend, H.W. Yu, K. Raju, P. Fitriani, D.H. Yoon, Tubular Si-infiltrated SiC_f/SiC composites for solar receiver application – Part 1: fabrication by replica and electrophoretic deposition, Sol. Energy Mater. Sol. Cells 132 (2015) 123-130. https://doi.org/10.1016/j.solmat.2014.08.029

[**26**] A. Ortona, C. D'Angelo, S. Gianella, D. Gaia, Cellular ceramics produced by rapid prototyping and replication, Mater. Lett. 80 (2012) 95-98. https://doi.org/10.1016/j.matlet.2012.04.050

[**27**] L. Wahl, M. Lorenz, J. Biggemann, N. Travitzky, Robocasting of reaction bonded silicon carbide structures, J. Eur. Ceram. Soc. 39 (2019) 4520-4526. https://doi.org/10.1016/j.jeurceramsoc.2019.06.049

[**28**] Z. Fu, L. Schlier, N. Travitzky, P. Greil, Three-dimensional printing of SiSiC lattice truss structures, Materials Science and Engineering: A 560 (2013) 851-856. https://doi.org/10.1016/j.msea.2012.09.107

[**29**] L. Schlier, W. Zhang, N. Travitzkyn P. Greil, J. Cypris, M. Weclas, Macro-Cellular Silicon carbide Reactors for Nonstationary Combustion Under Piston Engine-Like Conditions, Applied Ceramic Technology 8 [5] (2011) 1237-1245. https://doi.org/10.1111/j.1744-7402.2010.02591.x

[**30**] A. Fleisher, D. Zolotaryov, A. Kovalevsky, G. Muller-Kamskii, E. Eshed, M. Kazakin, V.V. Popov Jr., Reaction bonding of silicon carbides by Binder Jet 3D-Printing, phenolic resin binder impregnation and capillary liquid silicon infiltration, Ceram. Int. 45 (2019) 18023-18029. https://doi.org/10.1016/j.ceramint.2019.06.021

[**31**] A. Zocca, C. M. Gomes, A. Staude, E. Bernardo, J. Gunster, P. Colombo, SiOC ceramics with ordered porosity by 3D-printing of a preceramic polymer, J. Mater. Res. 28 (2013) 2243-2252. http://dx.doi.org/10.1557/jmr.2013.129

[**32**] E. Zanchetta, M. Cattaldo, G. Franchin, M. Schwentenwein, J. Homa, G. Brusatin, P. Colombo, Stereolithography of SiOC Ceramic Microcomponents, Adv. Mater. 28 (2016) 370-376. https://doi.org/10.1002/adma.201503470

[**33**] Y. De Hazan, D. Penner, SiC and SiOC ceramic articles produced by stereolithography of acrylate modified, J. Eur. Ceram. Soc. 37 (2017) 5205-5212. https://doi.org/10.1016/j.jeurceramsoc.2017.03.021

[34] L.L. Snead, T. Nozawa, Y. Katoh, T.-S. Byun, S. Kondo, D.A. Petti, Handbook of SiC properties for fuel performance modeling, J. Nucl. Mater. 371 (2007) 329-377. https://doi.org/10.1016/j.jnucmat.2007.05.016

[**35**] F. Christin, L. Héraud, J.J. Choury, R. Naslain, P. Hagenmuller, In-depth Chemical Vapor Deposition of SiC within porous carbon-carbon materials, Proccedings of the 3rd European Conference on Chemical Vapor Deposition, H.E. Hintermann ed., Neuchatel, Switzerland, 1980, pp. 154-161.

[36] F. Loumagne, F. Langlais, R. Naslain, S. Schamm, D. Dorignac, J. Sevely, Physicochemical properties of SiC-based ceramics deposited by low pressure CVD from CH_3SiCl_3-H_2, Thin Solid Films 254 (1995) 75-82. https://doi.org/10.1016/0040-6090(94)06237-F

[**37**] W.G. Zhang, K.J. Hüttinger, CVD of SiC from methyltricholrosilane. Part II: composition of the gas phase and the deposit, Chem. Vap. Deposition 7 (2001) 173-181. https://doi.org/10.1002/1521-3862(200107)7:4<173::AID-CVDE173>3.0.CO;2-X

[38] S. Kaur, R. Riedel, E. Ionescu, Pressureless fabrication of dense monolithic SiC ceramics from a polycarbosilane, J. Eur. Ceram. Soc. 34 (2014) 3571-3578. https://doi.org/10.1016/j.jeurceramsoc.2014.05.002

[39] R. Sreeja, B. Swaminathan, A. painuly, T.V. Sebastian, S. Packirisamy, Allylhydridopolycarbosilane (AHPCS) as matrix resin for C/SiC ceramic matrix composites, Mater. Sci. Eng. A. 168 (2010) 204-207. https://doi.org/10.1016/j.mseb.2009.12.033

[40] R. Naslain, Design, preparation and properties of non-oxide CMCs for application in engines and nuclear reactors: an overview, Com. Science & Tech. 64 (2004) 155-170. https://doi.org/10.1016/S0266-3538(03)00230-6

[41] A. Baux, L. Nouvian, K. Arnaud, S. Jacques, T. Piquero, D. Rochais, P. David, G. Chollon, Synthesis and properties of multiscale porosity TiC-SiC ceramics, J. Eur. Ceram. Soc. 39 (2019) 2601–2616. https://doi.org/10.1016/j.jeurceramsoc.2019.02.031

[42] ASTM E1876-01, Standard Test Method for Dynamic Young Modulus, Shear Modulus, and Poisson's Ratio by Impulse Excitation of Vibration. https://doi.org/10.1520/E1876-01

[43] ASTM C1684-13, Standard Test Method for Flexural Strength of Advanced Ceramics at Ambient Temperature-Cylindrical Rod Strength. https://doi.org/10.1520/C1684-13

[44] M. Dupeux, Introduction à la mécanique des structures, 2009, Paris: Dunod.

[45] R. Brezny, D.J. Green, C.Q. Dam, Evaluation of Strut Strength in Open-Cell Ceramics, J. Am. Ceram. Soc. 72 (1989) 885-889. http://dx.doi.org/10.1111/j.1151-2916.1989.tb06239.x

[46] M. Bougoin, D. Castel, F. Levallois, CTE homogeneity, isotropy and reproducibility in large parts made of sintered SiC, Proceedings of the International Conference on Space Optics, Volume 10564, ICSO-2012, 2017, 1056410. https://doi.org/10.1117/12.2309208

[47] L. Charpentier, C. Caliot, P. David, A. Baux, C. Heisel, D. Rochais, T. Chartier, Influence of the porosity of SiC on its optical properties and oxidation kinetics, AIP Conference Proceedings. 2126 (2019) 030013. https://doi.org/10.1063/1.5117525

[48] M. Balat-Pichelin, A. Bousquet, Total hemispherical emissivity of sintered SiC up to 1850 K in high vacuum and in air at different pressures, J. Eur. Ceram. Soc. 38 (2018) 3447-3456. https://doi.org/10.1016/j.jeurceramsoc.2018.03.050

[49] D. Rochais, H. Le Houëdec, F. Enguehard, J. Jumel, F. Lepoutre, Microscale thermal characterization at temperatures up to 1000 °C by photoreflectance microscopy. Application to the characterization of carbon fibres, J. Phys. D: Appl. Phys. 38 (2005) 1498-1503. http://dx.doi.org/10.1088/0022-3727/38/10/002

[50] D. Rochais, G. Le Meur, V. Basini, G. Domingues, Microscopic thermal characterization of HTR particle layers, Nucl. Eng. Des. 238 (2008) 3047–3059. https://doi.org/10.1016/j.nucengdes.2007.11.025

[51] B. Hay, S. Barré, J.R. Filtz, M. Jurion, D. Rochais, P. Sollet, New apparatus for thermal diffusivity and specific heat measurements at very high temperature, Int. J. Thermophys. 27 (2006) 1803-1815. https://doi.org/10.1007/s10765-006-0120-8

[52] G. Neuer, Spectral and Total Emissivity Measurement of Highly Emitting Material, Int. J. Thermophys. 16 (1995) 257-265. https://doi.org/10.1007/BF01438976

[53] T. Hirai, M. Sasaki, Silicon Carbide Prepared by Chemical Vapor Deposition, in Silicon Carbide Ceramics – 1, Fundamental and Solid Reaction, eds.S. Somiya, Y. Inomata, Elsevier Science Publishing Co. Inc., New York, USA, pp. 77-98.

[54] F. Tuinstra, J.L. Koenig, Raman spectrum of graphite, J. Chem. Phys. 53 (1970) 1126-1130. https://doi.org/10.1063/1.1674108

[55] A. Cuesta, P. Dahmelincourt, J. Laureyns, A. Martinez-Alonzo, J.M.D. Tascon, Raman microprobe study on carbon materials, Carbon 32 (1994) 1523-1532. http://dx.doi.org/10.1039/A805841E

[56] A.R. Puerta, E.E. Remsen, M.G. Bradley, W. Sherwood, L.G. Sneddon, Synthesis and ceramic conversion reactions of 9-BBN-modified allylhydridopolycarbosilane: A new single-source precursor to boron-modified silicon carbide, Chem. Mater. 15 (2003) 478-485. https://doi.org/10.1021/cm020697i

[57] S.C. Zunjarrao, A. Rahman, R.P. Singh, Characterization of the Evolution and Properties of Silicon Carbide Derived From a Preceramic Polymer Precursor, J. Am. Ceram. Soc. 96 (2013) 1869-1876. http://dx.doi.org/10.1111/jace.12273

[58] K.V. Moraes, L.V. Interrante, Processing, fracture toughness, and Vickers hardness of allylhydridopolycarbosilane-derived silicon carbide, J. Am. Ceram. Soc. 86 (2003) 342-346. https://doi.org/10.1111/j.1151-2916.2003.tb00020.x

[59] D.W. Feldman, J.H. Parker, W.J. Choyke, L. Patrick, Raman Scattering in 6H SiC, Phys. Rev. 170 (1968) 698-704. https://doi.org/10.1103/PhysRev.170.698

[60] Y. Ward, R.J. Young, R.A. Shatwell, Microstructural study of silicon carbide fibres through the use of Raman microscopy, J. Mater. Sci. 36 (2001) 55-66. https://doi.org/10.1023/A:1004830505979

[61] E. López-Honorato, C. Brigden, R.A. Shatwell, H. Zhang, I. Farnan, P. Xiao, P.Guillermier, J. Somers, Silicon carbide polytype characterisation in coated fuel particles by Raman spectroscopy and 29Si magic angle spinning NMR, J. Nucl. Mater. 433 (2013) 199-205. https://doi.org/10.1016/j.jnucmat.2012.08.047

[62] Y. Sasaki, Y. Nishina, M. Sato, K. Okamura, Raman study of SiC fibers made from polycarbosilane. J. Mater. Sci. 22 (1987) 443-448. https://doi.org/10.1007/BF01160751

[63] T.R. Watkins, D.J. Green, E.R. Ryba, Determination of Young's modulus in chemically vapor-deposited SiC coatings, J. Am. Ceram. Soc. 76 (1993) 1965-1968. http://dx.doi.org/10.1111/j.1151-2916.1993.tb08318.x

[64] C. Polzin, D. Günther, 3D Printing of Porous Al_2O_3 and SiC ceramics, Journal of Ceramic Science and Technology 6 (2015) 141-146. https://doi.org/10.4416/JCST2015-00013.

[65] Y.S. Touloukian, R.K. Kirby, E.R. Taylor, T.Y.R. Lee, Thermophysical Properties of Matter - the TPRC Data Series. Volume 13. Thermal Expansion - Nonmetallic Solids, IFI/Plenum Publishing Corp., New York USA, 1977, pp. 873-878. https://apps.dtic.mil/docs/citations/ADA129116

[66] S. Ghabezloo, Micromechanical analysis of the effect of porosity on the thermal expansion coefficient of heterogeneous porous materials, Int. J. Rock Mech. Min. Sci. 55 (2012) 97-101. https://doi.org/10.1016/j.ijrmms.2012.07.001

[67] W.G. Spitzer, D. Kleinman, D. Walsh, Infrared Properties of Hexagonal Silicon Carbide, Phys. Rev. 113 (1959) 127-132. https://doi.org/10.1103/PhysRev.113.127

[68] C.P. Cagran, L.M. Hanssen, M. Noorma, A.V. Gura, S.N. Mekhontsev, Temperature-Resolved Infrared Spectral Emissivity of SiC and Pt–10Rh for Temperatures up to 900 °C, Int. J. Thermophys. 28 (2007) 581-597. http://dx.doi.org/10.1007/s10765-007-0183-1

[69] F. Wang L. Cheng, L. Xiang, Q. Zhang, L. Zhang, Effect of SiC coating and heat treatment on the thermal radiation properties of C/SiC composites, J. Eur. Ceram. Soc. 34 (2014) 1667-1672. https://doi.org/10.1016/j.jeurceramsoc.2013.12.012

[70] G. Neuer, G. Jaroma-Weiland, Spectral and Total Emissivity of High-Temperature Materials, International Journal of Thermophysics 19 (1998) 917-929. https://doi.org/10.1023/A:1022607426413

[71] P.J. Jorgensen, M.E. Wadsworth, I.B. Cutler, Oxidation of Silicon Carbide, J. Am. Ceram. Soc. 42 (1959) 613–616. http://dx.doi.org/10.1111/j.1151-2916.1959.tb13582.x

[72] T. Narushima, T. Goto, Y. Igushi, T. Hirai, High-temperature active oxidation of chemically vapor-deposited silicon carbide in an Ar-O_2 atmosphere, J. Am. Ceram. Soc. 74 (1991) 2583-2586. https://doi.org/10.1111/j.1151-2916.1991.tb06803.x

[73] J.A. Costello, R.E. Tressler, Oxidation kinetics of hot-pressed and sintered α-SiC, J. Am. Ceram. Soc. 64 (1981) 327-331. https://doi.org/10.1111/j.1151-2916.1965.tb14728.x

[74] J.A Costello, R.E. Tressler, Oxidation kinetics of silicon carbide crystals and ceramics: I, in dry oxygen, J. Am. Ceram. Soc. 69 (1986) 674-681. https://doi.org/10.1111/j.1151-2916.1986.tb07470.x

[75] D.P. Hasselman, Unified theory of Thermal shock fracture initiation and crack propagation in brittle ceramics, stress resistance of Engineering ceramics, J. Am. Ceram. Soc. 52 (1969) 600-604. https://doi.org/10.1111/j.1151-2916.1969.tb15848.x

[76] D.P. Hasselman, Thermal stress resistance of Engineering ceramics, Mater. Sci. Eng. A 71 (1985) 251-264. https://doi.org/10.1016/0025-5416(85)90235-6

[77] M. Cannio, D.N. Boccaccini, M. Romagnoli, New methods for the assessment of thermal shock resistance in refractory materials, pp. 3293-3307, in Encyclopedia of Thermal Stresses, ed. R.B. Hetnarski, 2014. https://doi.org/10.1007/978-94-007-2739-7_34

[78] J. Wu, M. Liu, X. Xu, Y. Zhang, X. Lao, A Novel Si_3N_4–SiC Ceramic Used for Volumetric Receivers, Int. J. Appl. Ceram. Technol. 11 (2014) 246-253. http://dx.doi.org/10.1111/ijac.12094

[79] M.I. Roldán, O. Smirnova, T. Fend, J.L. Casas, E. Zarza, Thermal analysis and design of a volumetric solar absorber depending on the porosity, Renewable Energy 62 (2014) 116-128. http://dx.doi.org/10.1016/j.renene.2013.06.043

Tables

Table 1. Experimental conditions for CVI and CVD

	T (°C)	P_{total} (mbar)	Q_{MTS} (sccm)	Q_{H_2} (sccm)	t (h)
CVI	950	50	60	180	4
CVD	1200	100	200	600	6

Table 2. Atomic concentration (%) of C, Si and O in each constituent of the CVI/CVD lattice structure, as measured by EPMA

	C (at. %)	Si (at. %)	O (at. %)
α-SiC particles	49.0 ± 0.5	50.6 ± 0.5	0.4 ± 0.2
CVD-SiC	50.3 ± 0.5	49.5 ± 0.5	0.2 ± 0.2
PDC	49.9 ± 0.5	41.3 ± 0.5	8.8 ± 0.8

Table 3. True density (as measured by He-pycnometry), apparent density (as measured by Hg-porosimetry), residual open porosity (as measured by He-pycnometry and X-ray tomography) and specific surface area of the PIP, CVI and CVI/CVD lattices structures

	ρ_{true}^{He} (g/cm^3)	ρ_{app}^{Hg} (g/cm^3)	P_{pycno} (%)	P_{tomo} (%)	S_s (m²/g)
PIP	3.00 ± 0.05	1.3	57 ± 2	60 ± 4	1.1
CVI	2.80 ± 0.03	1.8	36 ± 2	-	-
CVI/CVD	3.00 ± 0.05	2.6	13 ± 2	14 ± 2	< 0.3*

*0.3 m²/g is the limit of quantification

Table 4. Mechanical properties of the rods.

	E_{acou} (GPa)	E_{bend} (GPa)	σ_{bend} (MPa)
PIP	-	4.9 ± 1.4	6.3 ± 2
CVD	201 ± 12	136 ± 13	101 ± 30

Table 5. Bending failure stresses of the various heat-treated CVD rods

	70 thermal cycles (90 s heating up to ≈ 900 °C + natural cooling for 90 s)	One long single cycle (70 min heating at ≈ 900 °C + natural cooling)	TGA (1200 °C, 50 h in dry air)
σ_{ben} (MPa)	91	136	82
E_{bend} (GPa)	83	116	125

Figure captions

Fig. 1. Specimens processed and tested: (a) cubic unit cell (b) cellular lattice structures, (c) rods, (d) circular plates

Fig. 2. (a) Global view of the device used for the single strut tearing tests, (b) cellular lattice structure and nylon thread positioning in the specimen holder, (c) schematic showing the tested strut, neighboring nodes and specimen holder window positioning

Fig. 3 (a) Schematic of the device used for the thermal shock and fatigue tests in air (b) platinum wire heating during the test of an alumina rod, (c) example of 2D temperature map recorded with the InSb infrared camera

Fig. 4. SEM images (SE mode) of a strut: (a) and (b) as-printed lattice structure, (b) and (e) lattice structure after CVI, (c) and (f) lattice structure after CVI and CVD

Fig. 5. (a) Raman spectra of the PDC parts in the lattice structures at various stages of the process, (b) Raman spectra of an α-SiC particle, the CVI and the CVD-SiC coating in the lattice structures.

Fig. 6. Strut cross-section in a CVI lattice structure: (a) overview, (b) close view near the surface, (c) close view of the core

Fig. 7. Strut cross-section in a CVI/CVD lattice structure: (a) overview, (b) close view near the surface, (c) close view of the core

Fig. 8. Pore size distribution in the PIP and CVI/CVD lattice structures, as measured by Hg-porosimetry

Fig. 9. X-ray tomography images of the PIP lattice structure: (a) overall perspective view obtained at low resolution (23 µm), (b) perspective view at high resolution (2 µm) of a node and its neighboring struts, (c) example of a greyscale image of a strut cross-section, (d) equivalent threshold image

Fig. 10. X-ray tomography images of the CVI/CVD lattice structure: (a) overall perspective view obtained at low resolution (23 µm), (b) perspective view at high resolution (2 µm) of a node and its neighboring struts, (c) example of a greyscale image of a strut cross-section, (d) equivalent threshold image

Fig. 11. (a) PIP and (b) CVI/CVD lattice structures after the single strut tearing tests: the locations of tested struts and the corresponding tearing forces are indicated on the pictures

Fig. 12. Load-displacement curves of the PIP and CVD rods recorded during the four-point bending tests

Fig. 13. (a) Thermal strain ε and (b) thermal expansion coefficient α of the PIP and CVI/CVD lattice structures, as measured by thermomechanical analysis

Fig. 14. Spectral emissivity at 300 K of the PIP and CVI/CVD specimens

Fig. 15. Optical properties the PIP and CVI/CVD specimens as a function of temperature

Fig. 16. Optical microscope image of a cross-section of a CVI/CVD lattice structure showing the different SiC-based components and the pump beam spot focused on a PDC part. The

darkest zones correspond to pores, brown regions to PDC parts and lightest zones to α-SiC particles and the CVD-SiC coating

Fig. 17. Thermal micro-diffusivity measurements on a PDC part: (a) attenuation, (b) phase shift 2D mappings recorded at 20 °C and a frequency of 150 kHz, (c) and (d) isoamplitude lines fit obtained. The thermal anisotropy factor deduced is equal to 1.02

Fig. 18. Thermal micro-diffusivity measurements on a PDC part: (a) attenuation and (b) phase shift 1D profiles recorded at 20 °C and 200 kHz, with related least square adjustments

Fig. 19. Thermal micro-diffusivity measurements on CVD-SiC: (a) attenuation and (b) phase shift profiles recorded at 20 °C and 1 MHz, with related least square adjustments

Fig. 20. Thermal diffusivity (a) and thermal conductivity (b) of the PIP and CVI/CVD specimens as a function of temperature

Fig. 21. (a) Relative weight change in dry air as a function of time recorded for the reference α-SiC powder, the PIP lattice structure and the CVI/CVD lattice structure. (b) Square of the relative weight change as a function of time recorded for the α-SiC powder and the PIP lattice structure, during the isothermal plateau at 1200 °C. (c) Relative weight change in dry air as a function of time recorded for the CVI/CVD lattice structure (closer view of the data presented in Fig. 21.a)

Fig. 22. Relative weight change in dry air as a function of time for a CVD rod

Fig. 23. Thermal shock and fatigue tests in air: apparent temperature profile along the CVD rod and the heating Pt coil, as extracted from 2D temperature mapping obtained with the IR Camera (see inset)

Fig. 24. Thermal shock and fatigue tests in air: temperature changes as a function of time, as recorded from the CVD rod and the Pt coil during thermal cycling

Supplementary material

SupMat 1 (a) Schematic of the 4-point bending test, (b) side view of the 4-point bending device, (c) example of a picture exploited by image correlation

SupMat 2: (a) Schematic and (b) upper view of the testing device used for acoustic analysis

SupMat 3: Example acoustic resonance spectrum showing the two natural frequencies of a CVD rod having an elliptical cross-section

SupMat 4: Close view of thermomechanical device used for the thermal strain thermal expansion coefficient measurements (Fig. 16)

SupMat 5: Cross-section of a rod after CVD, as examined by optical microscopy (overall section (a), core region (b), near surface region (c)) and X-ray tomography (overall perspective view (d), greyscale image of the cross-section (e), equivalent threshold image (f))

SupMat 6: Maximal stress-strain curve of the PIP and CVD material, as calculated from the load-displacement curves recorded during the four-point bending tests of the rods (see Fig. 12)

Supplementary material

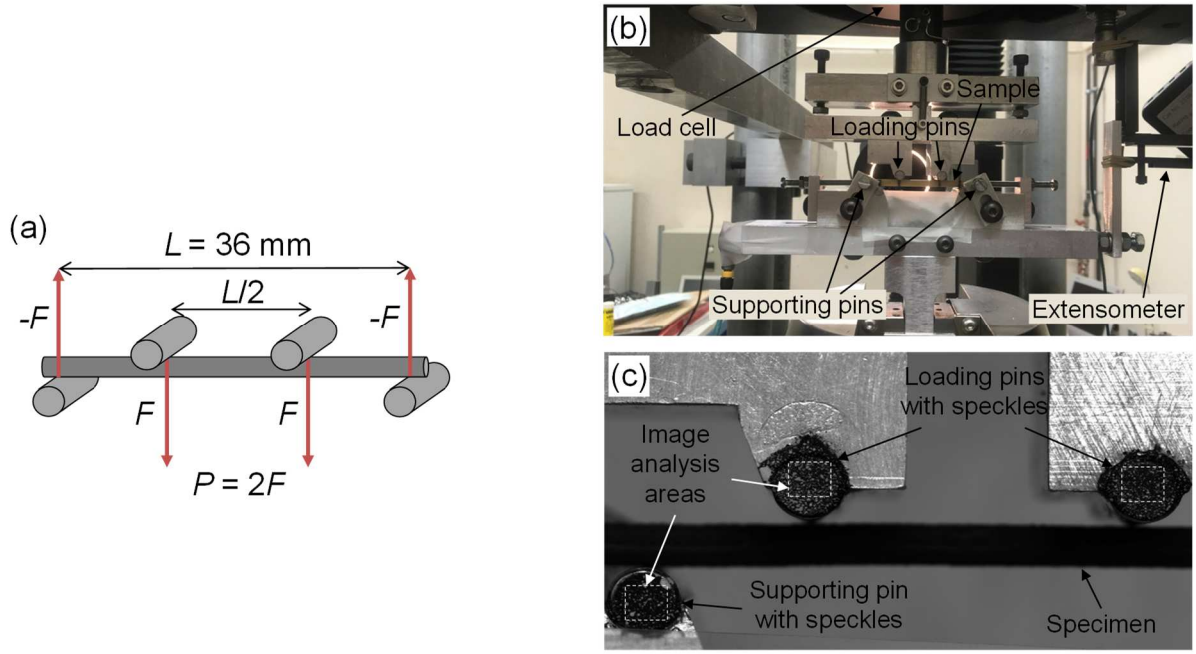

SupMat 1 (a) Schematic of the 4-point bending test, (b) side view of the 4-point bending device, (c) example of a picture exploited by image correlation

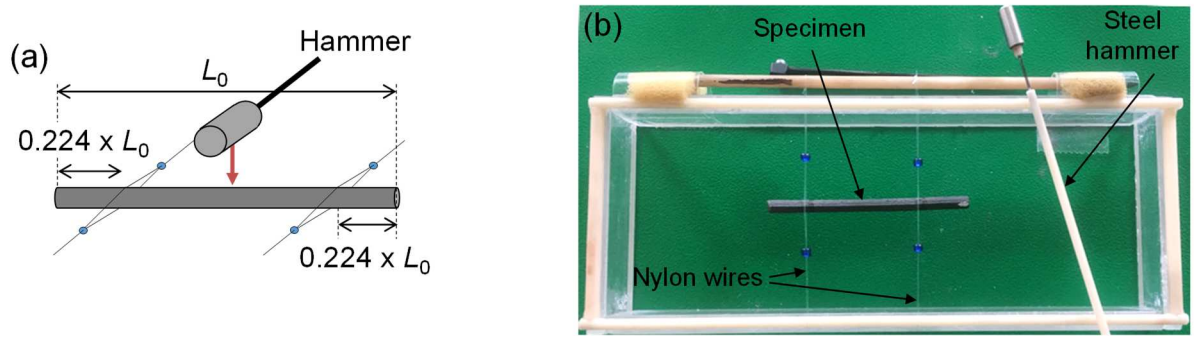

SupMat 2: (a) Schematic and (b) upper view of the testing device used for acoustic analysis

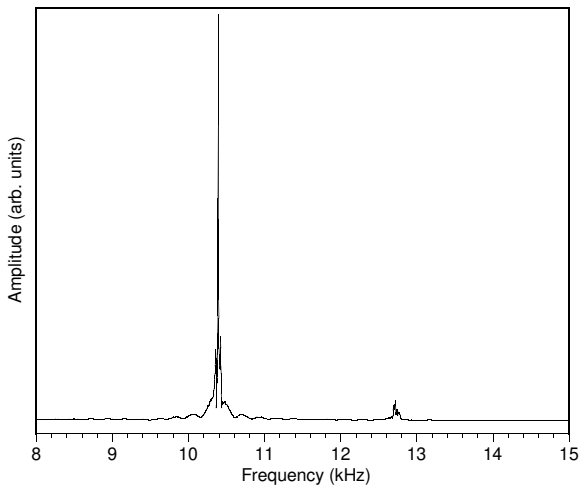

SupMat 3: Example acoustic resonance spectrum showing the two natural frequencies of a CVD rod having an elliptical cross-section

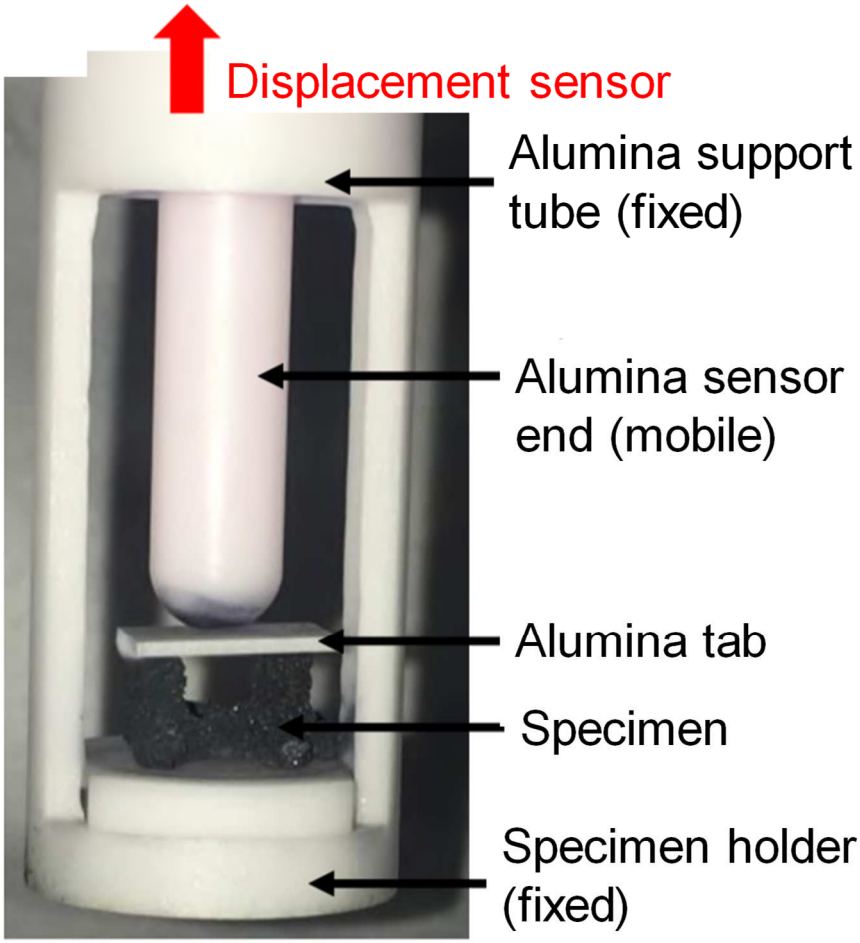

SupMat 4: Close view of thermomechanical device used for the thermal strain thermal expansion coefficient measurements (Fig. 16)

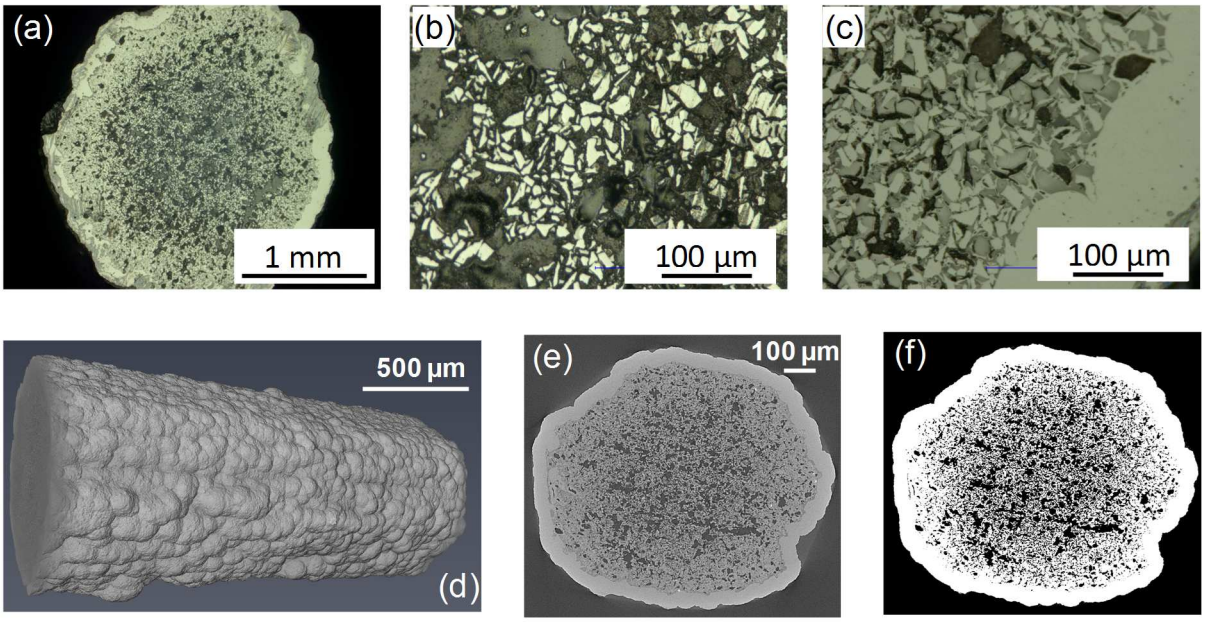

SupMat 5: Cross-section of a rod after CVD, as examined by optical microscopy (overall section (a), core region (b), near surface region (c)) and X-ray tomography (overall perspective view (d), greyscale image of the cross-section (e), equivalent threshold image (f))

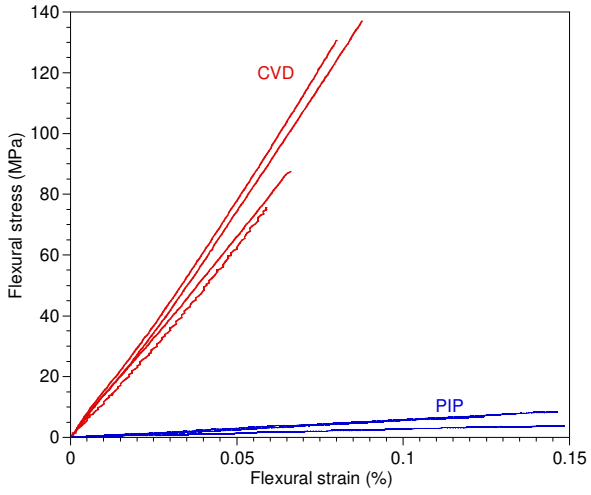

SupMat 6: Maximal stress-strain curve of the PIP and CVD material, as calculated from the load-displacement curves recorded during the four-point bending tests of the rods (see Fig. 12)

T (K)	C_p ($Jkg^{-1}K^{-1}$)	
	PIP	CVD
293	730	730
473	1040	1020
673	1190	1220
873	1200	1210
1073	1230	1230
1273	1230	1230

SupMat 7: C_p values as a function of temperature, as measured by differential thermal calorimetry